

Limits on statistical anisotropy from BOSS DR12 galaxies using bipolar spherical harmonics

Naonori S. Sugiyama^{1*}, Maresuke Shiraishi^{2,1}, and Teppei Okumura³

¹ *Kavli Institute for the Physics and Mathematics of the Universe (WPI),*

Todai Institutes for Advanced Study, The University of Tokyo, Chiba 277-8582, Japan

² *Department of General Education, National Institute of Technology, Kagawa College,*
355 Chokushi-cho, Takamatsu, Kagawa 761-8058, Japan

³ *Institute of Astronomy and Astrophysics, Academia Sinica, P. O. Box 23-141, Taipei 10617, Taiwan*

ABSTRACT

We measure statistically anisotropic signatures imprinted in three-dimensional galaxy clustering using bipolar spherical harmonics (BipoSHs) in both Fourier space and configuration space. We then constrain a well-known quadrupolar anisotropy parameter g_{2M} in the primordial power spectrum, parametrized by $P(\vec{k}) = \bar{P}(k)[1 + \sum_M g_{2M} Y_{2M}(\hat{k})]$, with M determining the direction of the anisotropy. Such an anisotropic signal is easily contaminated by artificial asymmetries due to specific survey geometry. We precisely estimate the contaminated signal and finally subtract it from the data. Using the galaxy samples obtained by the Baryon Oscillation Spectroscopic Survey Data Release 12, we find no evidence for violation of statistical isotropy, g_{2M} for all M to be of zero within the 2σ level. The g_{2M} -type anisotropy can originate from the primordial curvature power spectrum involving a directional-dependent modulation $g_*(\hat{k} \cdot \hat{p})^2$. The bound on g_{2M} is translated into g_* as $-0.09 < g_* < 0.08$ with a 95% confidence level when \hat{p} is marginalized over.

Key words: cosmology: large-scale structure of Universe – cosmology: dark matter – cosmology: observations – cosmology: theory

1 INTRODUCTION

The standard theory of inflation (Starobinsky 1980; Sato 1981; Guth 1981; Linde 1982; Albrecht & Steinhardt 1982) provides a highly successful mechanism for generating primordial density perturbations. The resulting perturbations are distributed as a statistically homogeneous, isotropic, parity-symmetric, and Gaussian random field. They provide the required seeds for the large-scale structure (LSS), after giving rise to temperature and polarization anisotropies in the cosmic microwave background (CMB) radiation, in excellent agreement with observation (Bennett et al. 1996; Hinshaw et al. 2013; Planck Collaboration et al. 2016a; Eisenstein et al. 2005; Alam et al. 2016). Conversely, testing these fundamental properties is crucial in improving our understanding of the physics of the Universe and will provide us with hints for new physics.

The aim of this paper is to test a minimal deviation from the standard inflation model, a violation of statistical isotropy (SI) with preserving the other

statistical properties of primordial fluctuations, using three-dimensional (3D) spectroscopic galaxy data of LSS surveys. We will focus especially on the so-called quadrupolar anisotropy (Ackerman et al. 2007), which is the simplest type of anisotropy that emerges from anisotropic inflation models in the limit of very weak anisotropy (e.g., Dimopoulos (2006); Dimopoulos & Karčiauskas (2008); Yokoyama & Soda (2008); Bartolo et al. (2009a,b); Himmetoglu et al. (2009a,b); Dimopoulos et al. (2010); Gümrükçüoğlu et al. (2010); Watanabe et al. (2010); Soda (2012); Bartolo et al. (2013a, 2015a,b); Naruko et al. (2015); Ashoorioon et al. (2016)) or an inflating solid or elastic medium (Bartolo et al. 2013b, 2014). The quadrupolar-type anisotropy is usually characterized by a parameter, g_{2M} or g_* (see Section 2 and Section 7 for their definitions, respectively). Up to now, there are many constraints on the quadrupolar parameters, g_{2M} and g_* , in CMB experiments (Groeneboom & Eriksen 2009; Groeneboom et al. 2010; Hanson & Lewis 2009; Bennett et al. 2011, 2013; Kim & Komatsu 2013; Planck Collaboration et al. 2016b,c; Ramazanov et al. 2017) and in two-dimensional (2D) photometric catalogs of LSS (Pullen & Hirata 2010), yielding $|g_{2M}| \lesssim 10^{-2}$ (10^{-1}) from CMB (LSS). We should stress

* E-mail: nao.s.sugiyama@gmail.com

here that all of these observations are based on 2D analysis and test isotropy after projection along the line-of-sight (LOS). In contrast, a direct analysis on the 3D clustering will be free from the information loss due to the projection, achieving a more accurate test.

Our previous work (Shiraishi et al. (2017), hereafter S17) has proposed an application of bipolar spherical harmonics (BipoSHs; Varshalovich et al. (1988); Hajian & Souradeep (2003); Hajian et al. (2004); Hajian & Souradeep (2006)) to the redshift-space galaxy power spectrum and two-point correlation function treated in full 3D space. The power spectrum depending on two directions, wavevector \vec{k} and the LOS direction \hat{n} , can be generally expanded in the BipoSH basis functions $\{Y_{\ell_1}(\hat{k}) \otimes Y_{\ell_2}(\hat{n})\}_{LM}$, which are tensor products of spherical harmonics with two different arguments. The remarkable feature of the BipoSH formalism is to parameterize departures from SI regarding total angular momenta L and M . In the absence of the assumption of SI, the corresponding expansion coefficients (hereafter, the BipoSH coefficients) yield the $L \geq 1$ modes, while SI induces the $L = 0$ mode alone. The BipoSH formalism can be therefore used to search for departures from SI and is always possible to translate any specific model for anisotropy. In S17, we have found that the $L = 2$ mode is simply proportional to the quadrupolar parameter g_{2M} in linear theory.

This work, for the first time, applies the BipoSH formalism to a publicly available 3D redshift survey data, the LOWZ and CMASS galaxy samples in both the North Galactic Cap (NGC) and the South Galactic Cap (SGC) derived from the Baryon Oscillation Spectroscopic Survey Data Release 12 (BOSS DR12; Alam et al. (2015)). We measure the $L = 2$ mode of the BipoSH coefficients for both the power spectrum and the correlation function. We then constrain the anisotropy parameters, g_{2M} and g_* , by comparing the measurements of the $L = 2$ mode with their theoretical predictions developed in S17. Combining all the BOSS samples, CMASS and LOWZ, we find no evidence for violation of SI, namely g_{2M} for all M to be of zero within the 2σ level and $-0.09 < g_* < 0.08$ with 95% probability, which is a more stringent constraint than the previous 2D analysis (Pullen & Hirata 2010), as expected.

To reach the goal, we go through the following two steps. First, we develop an estimator of the BipoSH coefficients of both the power spectrum and the correlation function. Since the $L = 0$ mode of the BipoSH coefficients reproduces the commonly used Legendre expansion coefficients (hereafter, the Legendre coefficients), our estimator can be regarded as a generalized one of the Legendre coefficients estimator (Landy & Szalay 1993; Feldman et al. 1994; Yamamoto et al. 2006; Bianchi et al. 2015; Scoccimarro 2015). Second, we discuss tools for studying the effects of survey geometry asymmetry on the observed BipoSH coefficients. Survey geometry asymmetries result in statistically anisotropic density fields. The asymmetries for their effects on the Legendre coefficients have already been studied in literature. We here confirm that they also produce ‘‘mimic’’ statistical anisotropies, biasing the primordial signal that we want to know. Estimating leakages of the anisotropic signal to the BipoSH coefficients, we find that the survey geometry effects provide a complete and

sufficient explanation of the observed BipoSH coefficients, concluding a null detection of g_{2M} or g_* .

The plan of our paper is as follows. In Section 2, we briefly review the application of the BipoSH formalism to the galaxy power spectrum and correlation function discussed in S17. In Section 3, we summarize the galaxy sample data used in our analysis. In Section 4, we explain the technique to measure the BipoSH coefficients of the power spectrum and correlation function, followed by the treatment of the survey geometry effects in Section 5. Section 6 presents the measurements of the BipoSH coefficients and their covariance matrices. In Section 7, the results including constraints on the quadrupolar parameters, g_{2M} and g_* , are presented. In this paper, we typically display figures only for CMASS NGC. However, we repeat the same analysis for the other three galaxy samples, CMASS SGC, LOWZ NGC, and LOWZ SGC as that for CMASS NGC and constrain g_{2M} and g_* for all the four samples. We present a summary and conclusions in Section 8. We additionally provide three Appendices: Appendix A presents the constraints on the quadrupolar parameter with various modulation scale-dependences, Appendix B gives detailed derivations of equations used in our analysis, and Appendix C compares the standard deviation of the BipoSH coefficients estimated from mock catalogs with that computed by linear theory.

Throughout this paper we adopt a flat Λ CDM cosmology (Planck Collaboration et al. 2016a): $\Omega_m = 0.309$, $\Omega_\Lambda = 0.691$, $n_s = 0.9608$, and $H_0 = 100 h \text{ km s}^{-1} \text{ Mpc}^{-1}$ with $h = 0.68$. We use the best fitting values of $f\sigma_8$ and $b\sigma_8$ measured in Gil-Marín et al. (2016): $(f\sigma_8, b\sigma_8) = (0.392, 1.283)$ for LOWZ and $(0.445, 1.218)$ for CMASS.

2 THEORY

2.1 BipoSH decomposition

The theory of redshift space distortions (RSDs; see Hamilton (1998) for a review) is based on the redshift space to real space transformation,

$$\vec{x} = \vec{x}_r + \frac{\vec{v}(\vec{x}_r) \cdot \hat{x}_r}{aH} \hat{x}_r, \quad (1)$$

where \vec{x} is the three-dimensional coordinates of an observed galaxy, \vec{x}_r is the real-space position of the galaxy, $\hat{x}_r = \vec{x}_r/|\vec{x}_r|$ is a unit vector pointing to the galaxy from the origin, \vec{v} is the galaxy peculiar velocity, and H is the Hubble expansion parameter. Under the global plane parallel approximation, the redshift-space galaxy power spectrum P_g is characterized by wavevector \vec{k} and the LOS \hat{n} : $P_g = P_g(\vec{k}, \hat{n})$. We note here that under the approximation, RSDs do preserve statistical homogeneity (Hamilton 1998).

Any function depending on two directions can be expanded in spherical harmonics $Y_{\ell m}$ (e.g. Szapudi (2004)):

$$P_g(\vec{k}, \hat{n}) = \sum_{\ell m} \sum_{\ell' m'} P_{\ell m; \ell' m'}(k) y_{\ell m}(\hat{k}) y_{\ell' m'}(\hat{n}), \quad (2)$$

where $y_{\ell m} = \sqrt{4\pi/(2\ell+1)} Y_{\ell m}$ is a normalized spherical harmonic function, and the corresponding expansion coefficients (hereafter, the spherical harmonic coefficients)

$P_{\ell m; \ell' m'}(k)$ are given by

$$P_{\ell m; \ell' m'}(k) = (2\ell + 1)(2\ell' + 1) \int \frac{d^2 \hat{k}}{4\pi} \int \frac{d^2 \hat{n}}{4\pi} \times y_{\ell m}^*(\hat{k}) y_{\ell' m'}^*(\hat{n}) P_g(\vec{k}, \hat{n}). \quad (3)$$

As an alternative way to generally decompose the power spectrum, we apply the BipoSH expansion (Varshalovich et al. 1988; Hajian & Souradeep 2003; Shiraishi et al. 2017):

$$P_g(\vec{k}, \hat{n}) = \sum_{LM} \sum_{\ell\ell'} \mathcal{P}_{\ell\ell'}^{LM}(k) S_{\ell\ell'}^{LM}(\hat{k}, \hat{n}). \quad (4)$$

In the above expression, we defined a normalized BipoSH basis $S_{\ell\ell'}^{LM}(\hat{k}, \hat{n})$ as¹

$$S_{\ell\ell'}^{LM}(\hat{k}, \hat{n}) \equiv (-1)^M \sum_{mm'} \begin{pmatrix} \ell & \ell' & L \\ m & m' & -M \end{pmatrix} y_{\ell m}(\hat{k}) y_{\ell' m'}(\hat{n}), \quad (7)$$

where the matrices denote the Wigner 3- j symbols, and the BipoSH coefficients $\mathcal{P}_{\ell\ell'}^{LM}$ are then given by

$$\mathcal{P}_{\ell\ell'}^{LM}(k) = (2L + 1)(-1)^M \sum_{mm'} \begin{pmatrix} \ell & \ell' & L \\ m & m' & -M \end{pmatrix} P_{\ell m; \ell' m'}(k). \quad (8)$$

Throughout this paper, we use upper-case indices LM for statistical anisotropies in the power spectrum and correlation function.

For $L = 0$, the BipoSH coefficients $\mathcal{P}_{\ell\ell'}^{LM}$ are related to the Legendre coefficients:

$$\mathcal{P}_{\ell\ell'}^{00}(k) = \delta_{\ell\ell'} \sqrt{2\ell + 1} (-1)^\ell P_\ell(k), \quad (9)$$

where we used the relation $\begin{pmatrix} \ell & \ell' & 0 \\ m & m' & 0 \end{pmatrix} = \frac{(-1)^{\ell' - m}}{\sqrt{2\ell + 1}} \delta_{\ell\ell'} \delta_{m, -m'}$, and the Legendre coefficients P_ℓ are given by (Hamilton 1998)

$$P_\ell(k) = (2\ell + 1) \int \frac{d^2 \hat{k}}{4\pi} \int \frac{d^2 \hat{n}}{4\pi} \mathcal{L}_\ell(\hat{k} \cdot \hat{n}) P_g(\vec{k}, \hat{n}) \quad (10)$$

with Legendre polynomials \mathcal{L}_ℓ . In other words, the galaxy power spectrum can be written as

$$P_g(\vec{k}, \hat{n}) = \sum_{\ell} P_\ell(k) \mathcal{L}_\ell(\hat{k} \cdot \hat{n}) + \sum_{L \geq 1, M} \sum_{\ell\ell'} \mathcal{P}_{\ell\ell'}^{LM}(k) S_{\ell\ell'}^{LM}(\hat{k}, \hat{n}), \quad (11)$$

where we used $S_{\ell\ell'}^{00}(\hat{k}, \hat{n}) = \delta_{\ell\ell'} ((-1)^\ell / \sqrt{2\ell + 1}) \mathcal{L}_\ell(\hat{k} \cdot \hat{n})$. If SI is valid, then the power spectrum can be only described by the Legendre coefficients. However, the presence of statistical anisotropy produces additional terms other than the Legendre coefficients. Rotational asymmetry terms $P_{\ell\ell'}^{L \geq 1, M}$, i.e. non-zero total angular momenta, are orthogonal to the Legendre coefficients P_ℓ induced by the $L = 0$ mode, which

¹ The standard BipoSHs are given by

$$Y_{\ell\ell'}^{LM}(\hat{n}, \hat{n}') = \sum_{mm'} C_{\ell m; \ell' m'}^{LM} Y_{\ell m}(\hat{n}) Y_{\ell' m'}(\hat{n}'), \quad (5)$$

where $C_{\ell m; \ell' m'}^{LM} = (-1)^{\ell - \ell' + M} \sqrt{2L + 1} \begin{pmatrix} \ell & \ell' & L \\ m & m' & -M \end{pmatrix}$ denote the Clebsch-Gordan coefficients, and this standard BipoSHs are related to our normalized ones as follows:

$$Y_{\ell\ell'}^{LM}(\hat{n}, \hat{n}') = (-1)^{\ell - \ell'} \sqrt{\frac{(2L + 1)(2\ell + 1)(2\ell' + 1)}{(4\pi)^2}} S_{\ell\ell'}^{LM}(\hat{n}, \hat{n}'). \quad (6)$$

means that the $L \neq 0$ modes are unbiased observables of the rotational invariance breaking (Shiraishi et al. 2017).

For a practical analysis, S17 has defined a reduced BipoSH coefficients as

$$P_{\ell\ell'}^{LM}(k) \equiv H_{\ell\ell'}^L \mathcal{P}_{\ell\ell'}^{LM}(k), \quad (12)$$

where $H_{\ell\ell'}^L = \begin{pmatrix} \ell & \ell' & L \\ 0 & 0 & 0 \end{pmatrix}$ filters even $\ell + \ell' + L$ components. In this paper, we only focus on the even $\ell + \ell' + L$ components, because a simple model breaking SI that we use in our analysis leads to $\mathcal{P}_{\ell\ell'}^{LM} \propto H_{\ell\ell'}^L$, i.e. $P_{\ell\ell'}^{LM} \propto (H_{\ell\ell'}^L)^2$ (see equation (20)). We assume parity symmetry, i.e. invariance of the galaxy power spectrum under parity flip, $\vec{k} \rightarrow -\vec{k}$ and $\hat{n} \rightarrow -\hat{n}$, restricting allowed multipoles to $\ell + \ell' = \text{even}$. Therefore, our interests are only in the $L = \text{even}$ modes. Note that the filtering of $H_{\ell\ell'}^L$ provides a convenient normalization to reproduce the Legendre coefficients P_ℓ for $L = 0$:

$$P_{\ell\ell'}^{00}(k) = \delta_{\ell\ell'} P_\ell(k). \quad (13)$$

The two-point correlation function can be expanded in spherical harmonics

$$\xi(\vec{r}, \hat{n}) = \sum_{\ell m} \sum_{\ell' m'} \xi_{\ell m; \ell' m'}(r) y_{\ell m}(\hat{r}) y_{\ell' m'}(\hat{n}), \quad (14)$$

and we define the reduced BipoSH coefficients as

$$\xi_{\ell\ell'}^{LM}(r) \equiv (2L + 1) H_{\ell\ell'}^L (-1)^M \sum_{mm'} \begin{pmatrix} \ell & \ell' & L \\ m & m' & -M \end{pmatrix} \xi_{\ell m; \ell' m'}(r). \quad (15)$$

Here, the spherical and BipoSH coefficients, $\xi_{\ell m; \ell' m'}$ and $\xi_{\ell\ell'}^{LM}$, are related to the Fourier-space ones according to the following Hankel transformations:

$$\begin{aligned} \xi_{\ell m; \ell' m'}(r) &= i^\ell \int \frac{dk k^2}{2\pi^2} j_\ell(rk) P_{\ell m; \ell' m'}(k) \\ \xi_{\ell\ell'}^{LM}(r) &= i^\ell \int \frac{dk k^2}{2\pi^2} j_\ell(rk) P_{\ell\ell'}^{LM}(k), \end{aligned} \quad (16)$$

where j_ℓ is the spherical Bessel function of order ℓ . Similarly to the power spectrum, the Legendre coefficients of the correlation function correspond to $\xi_{\ell\ell'}^{00}$, given by

$$\xi_\ell(r) = \xi_{\ell\ell}^{00}(r) = i^\ell \int \frac{dk k^2}{2\pi^2} j_\ell(rk) P_\ell(k). \quad (17)$$

When the LOS direction is not determined by the global one \hat{n} but by observed galaxy positions, the redshift-space power spectrum and correlation function become inhomogeneous, even if the primordial curvature perturbation ζ satisfies statistical homogeneity $\langle \zeta(\vec{k}) \zeta(\vec{k}') \rangle = (2\pi)^3 \delta_{\text{D}}(\vec{k} + \vec{k}') P_\zeta(k)$. This RSD-induced translational asymmetry significantly affects the observed power spectrum and correlation function through survey window functions, which is discussed in more detail in Section 5.

2.2 Quadrupolar-type anisotropy

In linear theory, a galaxy power spectrum that breaks SI can be decomposed via (Shiraishi et al. 2017)

$$P_g(\vec{k}, \hat{n}) = P_K(\vec{k}) \left[1 + \sum_{L \geq 2} \sum_{M}^{L=\text{even}} g_{LM} f(k) Y_{LM}(\hat{k}) \right], \quad (18)$$

where P_K is the so-called Kaiser formula of linear RSD (Kaiser 1987),

$$P_K(\vec{k}) = ((b\sigma_8) + (f\sigma_8) \mu_k^2)^2 P_{\text{lin}}(k, z = 0), \quad (19)$$

where $\mu_k = \hat{k} \cdot \hat{n}$, σ_8 denotes the rms matter fluctuation on scales of $8 h^{-1}$ Mpc, b represents the linear bias parameter, $f\sigma_8 = d \ln \sigma_8 / d \ln a$ is the logarithmic growth rate multiplied by σ_8 , and P_{lin} is the isotropic, linear matter power spectrum. While b , σ_8 , and f are computed at given redshift z , P_{lin} is computed at $z = 0$. In the above expression, P_{lin} is normalized by σ_8^2 so that $\sigma_8(z = 0) = 1$, because in the standard definition of P_{lin} , it is proportional to σ_8^2 . One can thus see from equation (19) that the amplitude of the observed power spectrum is characterized by the combination of $b\sigma_8$ and $f\sigma_8$, and that the RSD effect makes the LOS direction special.

The additional direction dependence is represented by $\sum_{LM} g_{LM} f(k) Y_{LM}(\hat{k})$, where g_{LM} means the magnitude of statistical anisotropy on order L , with M giving the direction of that anisotropy. The anisotropy parameter g_{LM} satisfies a reality condition $g_{LM}^*(k) = (-1)^M g_{L,-M}$. The shape of the scale-dependence function of the primordial anisotropy, $f(k)$, depends strongly on the inflationary Lagrangian.² In this analysis, we will treat $f(k)$ as a power law, $f(k) = (k/k_0)^n$, and consider four values of the spectral index, namely $n = -2, -1, 0$, and 1 .³ As the main results, we ignore the scale dependence of $f(k)$ and focus only on $n = 0$, while we summarize the results for the other indexes, $n = -2, -1$, and 1 , in Appendix A.

Substituting the above equation (18) into equation (12) leads to

$$\begin{aligned} P_{\ell\ell'}^{00}(k) &= \delta_{\ell\ell'} P_{\ell'}(k) \\ P_{\ell\ell'}^{L \geq 2, M}(k) &= \sqrt{\frac{2L+1}{4\pi}} g_{LM} f(k) \\ &\times (2\ell+1) (H_{\ell\ell'}^L)^2 P_{\ell'}(k), \end{aligned} \quad (20)$$

where the Legendre coefficients $P_{\ell'}$ yield only the monopole $P_0 = ((b\sigma_8)^2 + (2/3)(b\sigma_8)(f\sigma_8) + (1/5)(f\sigma_8)^2) P_{\text{lin}}$, the quadrupole $P_2 = ((4/3)(b\sigma_8)(f\sigma_8) + (4/7)(f\sigma_8)^2) P_{\text{lin}}$, and the hexadecapole $P_4 = (8/35)(f\sigma_8)^2 P_{\text{lin}}$ in linear theory, and these satisfy a magnitude relation $|P_0| > |P_2| > |P_4|$ at large scales. As expected, each of the $L \geq 2$ modes is proportional to the corresponding anisotropy parameter g_{LM} , and the $L = 0$ mode reproduces the Legendre coefficients P_{ℓ} .

From now, we analyze the leading-order mode ($L = 2$) in equation (20), the so-called ‘‘quadrupolar anisotropy’’. The parity-even condition and the triangular inequality coming from the filter $H_{\ell\ell'}^{L=2}$ restricts the allowed coefficients in $P_{\ell\ell'}^{LM}$ to $(\ell, \ell') = (2, 0), (0, 2), (2, 2), (4, 2), (2, 4), (4, 4)$, and $(6, 4)$. S17 has shown that P_{20}^{2M} dominantly contributes to the signal-to-noise ratio, because P_{20}^{2M} is proportional to the monopole P_0 , while all the other terms are proportional to the quadrupole P_2 or the hexadecapole P_4 that is smaller than the monopole. Hence, we focus only on P_{20}^{2M} in our analysis, which is derived from equation (20),

$$P_{20}^{2M}(k) = \sqrt{\frac{5}{4\pi}} g_{2M} f(k) P_0(k). \quad (21)$$

In the same manner as the Fourier-space analysis, in the

configuration-space analysis we only consider $\xi_{20}^{2M}(r)$ given from equation (16) by

$$\xi_{20}^{2M}(r) = -\sqrt{\frac{5}{4\pi}} g_{2M} \int \frac{dk k^2}{2\pi^2} j_2(rk) f(k) P_0(k), \quad (22)$$

where we note here that $j_{\ell=2}$ is used, even though the power spectrum in the integrand is the monopole.

3 DATA

We use two galaxy samples, the LOWZ sample with 463044 galaxies between $z = 0.15$ - 0.43 ($z_{\text{eff}} = 0.33$) and the CMASS sample with 849637 galaxies between $z = 0.43$ - 0.7 ($z_{\text{eff}} = 0.56$) (White et al. 2011; Parejko et al. 2013; Bundy et al. 2015; Leauthaud et al. 2016; Saito et al. 2016). These samples are drawn from the Data Release 12 (DR12; Alam et al. (2015)) of the Baryon Oscillation Spectroscopic Survey (BOSS; Bolton et al. (2012); Dawson et al. (2013)), which is part of the Sloan Digital Sky Survey III (SDSS-III; Eisenstein et al. (2011)), and are selected from multi-color SDSS imaging (Fukugita et al. 1996; Gunn et al. 1998; Smith et al. 2002; Gunn et al. 2006; Doi et al. 2010).

To correct for several observational artifacts in the catalogs and obtain unbiased estimates of the galaxy density field, we use a completeness weight for each galaxy (Ross et al. 2012; Anderson et al. 2014; Reid et al. 2016),

$$w_c(\vec{x}) = w_{\text{sys tot}}(\vec{x}) (w_{\text{cp}}(\vec{x}) + w_{\text{noz}}(\vec{x}) - 1), \quad (23)$$

where \vec{x} is the observed galaxy position, and w_{cp} , w_{noz} , and $w_{\text{sys tot}}$ denote a redshift failure weight, a collision weight, and an angular systematics weight, respectively. The details about the observational systematic weights are described in Reid et al. (2016). Additionally, we use the optimal weighting of galaxies, so-called the FKP weight w_{FKP} (Feldman et al. 1994). We adopt the values of the FKP weight given in the publicly available DR12 galaxy and random catalogues, which are computed using the following amplitude of the power spectrum, $P_0 = 10^4 h^{-3} \text{Mpc}^3$. However, we do not expect that more appropriate values of P_0 will significantly improve the constraint on the anisotropy. By multiplying the completeness weight by the FKP weight, we finally define a local weight function that we use in our analysis:

$$w(\vec{x}) = w_c(\vec{x}) w_{\text{FKP}}(\vec{x}). \quad (24)$$

4 METHODOLOGY

In this section, we describe the estimators we use to measure the power spectrum and correlation function from the observed galaxy distribution.

The number density field of galaxies is given by

$$n(\vec{x}) = \sum_i^{N_{\text{gal}}} w(\vec{x}_i) \delta_{\text{D}}(\vec{x} - \vec{x}_i), \quad (25)$$

where \vec{x}_i represents the observed position of galaxy i , the weight function $w(\vec{x})$ is given by equation (24), N_{gal} denotes the total number of observed galaxies, and δ_{D} is a Dirac δ -function. To estimate the galaxy density fluctuation δn , we

² The linear growth rate f should be distinguished from this $f(k)$.

³ Such scale dependences are realized by, e.g., the running of an inflaton-vector coupling in vector inflation models (Bartolo et al. 2013a, 2015a,b).

measure the mean number density $\bar{n}(\vec{x})$ from a synthetic random catalog⁴, multiplied by a factor α ,

$$\bar{n}(\vec{x}) = \alpha \sum_i^{N_{\text{ran}}} w(\vec{x}_i) \delta_{\text{D}}(\vec{x} - \vec{x}_i), \quad (26)$$

where N_{ran} represents the total number of objects in the random catalog, and α is the ratio between the weighted numbers of galaxies in the real and random catalogs: $\alpha = \sum_i^{N_{\text{gal}}} w(\vec{x}_i) / \sum_i^{N_{\text{ran}}} w(\vec{x}_i) \sim 0.01$ in our analysis. By subtracting $\bar{n}(\vec{x})$ from $n(\vec{x})$, we obtain the observed galaxy density fluctuation

$$\delta n(\vec{x}) = n(\vec{x}) - \bar{n}(\vec{x}). \quad (27)$$

4.1 Power spectrum

In analogy to the estimator of the Legendre coefficients of the power spectrum (Feldman et al. 1994; Yamamoto et al. 2006), we present an estimator of $P_{\ell m; \ell' m'}$ (equation 3) as follows

$$\begin{aligned} \hat{P}_{\ell m; \ell' m'}(k) &= \frac{(2\ell+1)(2\ell'+1)}{A} \int \frac{d^2 \hat{k}}{4\pi} y_{\ell m}^*(\hat{k}) \int d^3 x_1 \int d^3 x_2 \\ &\times e^{-i\vec{k} \cdot \vec{x}_{12}} y_{\ell' m'}^*(\hat{n}_{12}) \delta n(\vec{x}_1) \delta n(\vec{x}_2), \end{aligned} \quad (28)$$

where $\vec{x}_{12} = \vec{x}_1 - \vec{x}_2$ is the relative coordinates of the pair of points \vec{x}_1 and \vec{x}_2 , the unit vector of $\vec{n}_{12} = (\vec{x}_1 + \vec{x}_2)/2$, denoted as \hat{n}_{12} , is used as the LOS direction to the pair, and A is the normalization factor given by

$$A = \int d^3 x \bar{n}^2(\vec{x}). \quad (29)$$

This normalization depends on a grid-cell resolution to compute the density field, and therefore, it is difficult to make A converge to a certain value in a large survey. However, this difficulty does not necessarily become an issue, because the value of A does not affect the final results as we will see in Section 5. The integral $\int d^2 \hat{k}$ in equation (28) is the angular integration, and it is performed over a spherical shell in Fourier space centered at each bin $k = |\vec{k}|$,

$$\int \frac{d^2 \hat{k}}{4\pi} = \frac{1}{N_k} \sum_{k-\Delta k/2 < k < k+\Delta k/2}, \quad (30)$$

where Δk is the bin size, and $N_k = 4\pi k^2 \Delta k V / (2\pi)^3$ is the number of independent Fourier modes with V being a given survey volume. Finally, equation (12) relates the estimator of $P_{\ell m; \ell' m'}$ to that of $P_{\ell \ell'}^{LM}$ through

$$\begin{aligned} \hat{P}_{\ell \ell'}^{LM}(k) &\equiv (2L+1) H_{\ell \ell'}^L(-1)^M \\ &\times \sum_{mm'} \binom{\ell \ell' L}{m m' -M} \hat{P}_{\ell m; \ell' m'}(k). \end{aligned} \quad (31)$$

In particular, for \hat{P}_{20}^{2M} we obtain

$$\begin{aligned} \hat{P}_{20}^{2M}(k) &= \hat{P}_{2M; 00}(k) \\ &= \frac{5}{A} \int \frac{d^2 \hat{k}}{4\pi} y_{2M}^*(\hat{k}) \left| \delta n(\vec{k}) \right|^2, \end{aligned} \quad (32)$$

⁴ For the random catalogs of the LOWZ and CMASS samples, we do not need the completeness weight in equation (23): $w_c = 1$.

where $\delta n(\vec{k})$ is the Fourier transform of $\delta n(\vec{x})$, given by

$$\delta n(\vec{k}) = \int d^3 x e^{-i\vec{k} \cdot \vec{x}} \delta n(\vec{x}). \quad (33)$$

To compute $\hat{P}_{\ell m; \ell' m'}$ and $\hat{P}_{\ell \ell'}^{LM}$, we apply the local plane parallel approximation $\hat{x}_1 \approx \hat{x}_2$, which is known to be rather accurate for the Legendre coefficients of the power spectrum P_ℓ (Samushia et al. 2015). This approximation allows the integrals in equation (28) to decouple into a product of Fourier transforms:

$$\begin{aligned} \hat{P}_{\ell m; \ell' m'}(k) &= \frac{(2\ell+1)(2\ell'+1)}{A} \int \frac{d^2 \hat{k}}{4\pi} y_{\ell m}^*(\hat{k}) \\ &\times \delta n_{\ell m}(\vec{k}) \delta n_{\ell' m'}^*(\vec{k}), \end{aligned} \quad (34)$$

where $\delta n_{\ell m}(\vec{k})$ is given by

$$\delta n_{\ell m}(\vec{k}) = \int d^3 x e^{-i\vec{k} \cdot \vec{x}} y_{\ell m}^*(\hat{x}) \delta n(\vec{x}). \quad (35)$$

The density fluctuation $\delta n(\vec{x})$ multiplied by $y_{\ell m}^*(\hat{x})$, which is denoted as $\delta n_{\ell m}(\vec{x})$, can be directly measured from a galaxy sample as,

$$\begin{aligned} \delta n_{\ell m}(\vec{x}) &= y_{\ell m}^*(\hat{x}) \delta n(\vec{x}) \\ &= \left(\sum_i^{N_{\text{gal}}} -\alpha \sum_i^{N_{\text{ran}}} \right) y_{\ell m}^*(\hat{x}_i) w(\vec{x}_i) \delta_{\text{D}}(\vec{x} - \vec{x}_i). \end{aligned} \quad (36)$$

Therefore, we stress here that $\delta n_{\ell m}(\vec{k})$ is computable using any fast Fourier transform (FFT) algorithm as the Fourier transform of $\delta n_{\ell m}(\vec{x})$. The computation of equation (34) then will be of $\mathcal{O}(N_k \ln N_k)$.

The FFT algorithm requires the interpolation of functions on a regular grid in position space. The Fourier transform of the density fluctuation measured by FFTs, $\delta n_{\ell m}(\vec{k})|_{\text{FFT}}$, includes the effect of the mass assignment function $W_{\text{mass}}(\vec{k})$ (Jing 2005). We can remove such effects from $\delta n_{\ell m}(\vec{k})|_{\text{FFT}}$ by simply dividing by $W_{\text{mass}}(\vec{k})$: $\delta n_{\ell m}(\vec{k}) = \delta n_{\ell m}(\vec{k})|_{\text{FFT}} / W_{\text{mass}}(\vec{k})$. The most popular mass assignment function is given by

$$W_{\text{mass}}(\vec{k}) = \prod_{i=x,y,z} \left[\text{sinc} \left(\frac{\pi k_i}{2k_{N,i}} \right) \right]^p, \quad (37)$$

where $k_{N,i} = \pi/H_i$ is the Nyquist frequency of i -axis with the grid spacing H_i on the axis. The indexes $p = 1$, $p = 2$, and $p = 3$ correspond to the nearest grid point (NGP), cloud-in-cell (CIC), and triangular-shaped cloud (TSC) assignment functions, respectively.

Finally, we need to subtract shot-noise terms from the BipoSH coefficients $\hat{P}_{\ell \ell'}^{LM}$ computed by equation (31). The shot-noise terms $S_{\ell \ell'}^{LM}$ on the BipoSH coefficients are given by

$$\begin{aligned} S_{\ell \ell'}^{LM}(k) &= (2L+1) H_{\ell \ell'}^L(-1)^M \\ &\times \sum_{mm'} \binom{\ell \ell' L}{m m' -M} S_{\ell m; \ell' m'}(k) \end{aligned} \quad (38)$$

with

$$\begin{aligned} S_{\ell m; \ell' m'}(k) &= \frac{(2\ell+1)(2\ell'+1)}{A} \int \frac{d^2 \hat{k}}{4\pi} y_{\ell m}^*(\hat{k}) \frac{C_{\text{shot}}(\vec{k})}{W_{\text{mass}}^2(\vec{k})} \\ &\times \left(\sum_i^{N_{\text{gal}}} + \alpha^2 \sum_i^{N_{\text{ran}}} \right) [w(\vec{x}_i)]^2 y_{\ell' m'}^*(\vec{x}_i). \end{aligned} \quad (39)$$

Here, the function $C_{\text{shot}}(\vec{k})$ has a simple analytic function given by equation (20) in Jing (2005).

The $L = 0$ mode of the BipoSH estimator $\widehat{P}_{\ell\ell'}^{LM}$ reproduces the Legendre coefficients estimator from equation (13),

$$\widehat{P}_\ell(k) = \widehat{P}_{\ell\ell}^{00}(k) = \frac{1}{2\ell+1} \sum_{m=-\ell}^{\ell} (-1)^m \widehat{P}_{\ell,-m;\ell m}(k), \quad (40)$$

where we used the relation $\mathcal{L}_\ell(\hat{x} \cdot \hat{y}) = \sum_m y_{\ell m}(\hat{x}) y_{\ell m}^*(\hat{y})$. Therefore, our BipoSH estimator can be used as an alternative to the standard FFT-based method to measure the multipole moments P_ℓ (Bianchi et al. 2015; Scoccimarro 2015). However, we stress here that one can measure P_ℓ with $\ell > 0$ faster using our estimator with the $L = 0$ mode (equation 40) than the standard one, because the BipoSH estimator requires a smaller number of FFTs to compute \widehat{P}_ℓ : \widehat{P}_ℓ can be measured by our estimator by $(2\ell+1)$ FFTs, while the standard one requires 1, 6 and 15 FFTs for $\ell = 0, 2$ and 4, respectively.

4.2 Two-point correlation function

Now we move onto the derivation of the estimator for the BipoSH coefficients of the two-point correlation function. To clarify the relation between the estimators of the power spectrum and the correlation function, we first present the estimator for the coefficients normalized by the factor A (equation 29), $\widehat{\xi}_{\ell\ell'}^{LM}|_A$:

$$\begin{aligned} \widehat{\xi}_{\ell\ell'}^{LM}(r)|_A &= (2L+1) H_{\ell\ell'}^L (-1)^M \\ &\times \sum_{mm'} \binom{\ell \ell' L}{m m' -M} \widehat{\xi}_{\ell m; \ell' m'}(r)|_A, \end{aligned} \quad (41)$$

where

$$\begin{aligned} \widehat{\xi}_{\ell m; \ell' m'}(r)|_A &= \frac{(2\ell+1)(2\ell'+1)}{A} \int \frac{d^2\hat{r}}{4\pi} y_{\ell m}^*(\hat{r}) \int d^3x_1 \int d^3x_2 \\ &\times \delta_D(\vec{r} - \vec{x}_{12}) y_{\ell' m'}^*(\hat{n}_{12}) \delta n(\vec{x}_1) \delta n(\vec{x}_2). \end{aligned} \quad (42)$$

A Hankel transform relates the above estimator $\widehat{\xi}_{\ell\ell'}^{LM}|_A$ to $\widehat{P}_{\ell\ell'}^{LM}$ (equation 31) as,

$$\widehat{P}_{\ell\ell'}^{LM}(k) = 4\pi(-i)^\ell \int dr r^2 j_\ell(kr) \widehat{\xi}_{\ell\ell'}^{LM}(r)|_A. \quad (43)$$

To compute $\widehat{\xi}_{\ell\ell'}^{LM}|_A$, we propose two ways, the pair-counting approach (e.g., Landy & Szalay 1993) and the FFT-based approach (e.g., Slepian & Eisenstein 2016). First, substituting equations (25) and (26) into equation (42) leads to the pair-counting estimator, reading

$$\begin{aligned} \widehat{\xi}_{\ell m; \ell' m'}(r)|_A &= \frac{(2\ell+1)(2\ell'+1)}{4\pi r^2 \Delta r A} \left(\sum_{i,j}^{N_{\text{gal}}} -2\alpha \sum_i^{N_{\text{gal}}} \sum_j^{N_{\text{ran}}} + \alpha^2 \sum_{i,j}^{N_{\text{ran}}} \right) \\ &\times \delta_K(r - |\vec{x}_{ij}|) y_{\ell m}^*(\hat{x}_{ij}) y_{\ell' m'}^*(\hat{n}_{ij}) w(\vec{x}_i) w(\vec{x}_j), \end{aligned} \quad (44)$$

where \hat{n}_{ij} and \hat{x}_{ij} are respectively the unit vectors of $\vec{n}_{ij} = (\vec{x}_i + \vec{x}_j)/2$ and $\vec{x}_{ij} = \vec{x}_i - \vec{x}_j$, δ_K is the Kronecker delta, and Δr is the bin size. The shot-noise term, which only contributes to a bin of $r = 0$, can be removed by not counting $i = j$ from the summations in equation (44), $\sum_{i,j}^{N_{\text{gal}}}$ and $\sum_{i,j}^{N_{\text{ran}}}$. Second, under the local plane parallel approximation

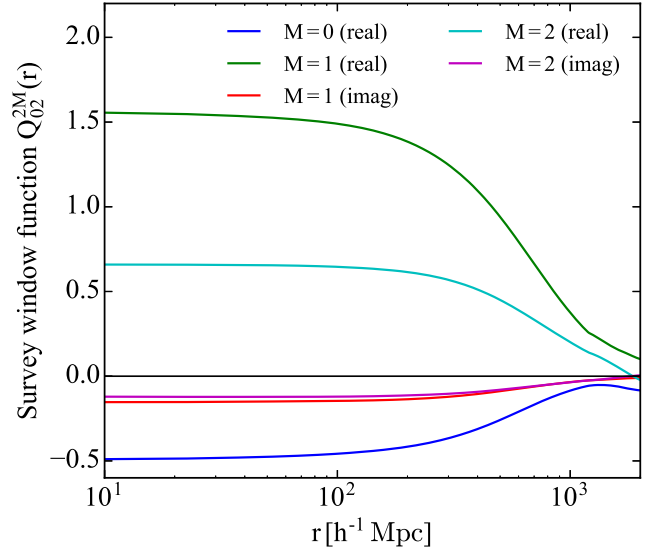


Figure 1. BipoSH coefficients of survey window functions Q_{20}^{2M} as given in equation (54) for CMASS NGC, which are used to compute the masked power spectrum and correlation function given by equations (60) and (61), respectively. They represent survey geometry asymmetries and result in statistical anisotropic signals on the BipoSH coefficients of the power spectrum and correlation function.

$\hat{x}_1 \approx \hat{x}_2$, the correlation function can be computed by FFTs

$$\begin{aligned} \widehat{\xi}_{\ell m; \ell' m'}(r)|_A &= \frac{(2\ell+1)(2\ell'+1)}{A} \int \frac{d^2\hat{r}}{4\pi} y_{\ell m}^*(\hat{r}) \int \frac{d^3k}{(2\pi)^3} e^{i\vec{k}\cdot\vec{r}} \\ &\times \left[\delta n_{\ell' m'}(\vec{k}) \delta n^*(\vec{k}) - S_{\ell' m'}(\vec{k}) \right], \end{aligned} \quad (45)$$

where the shot-noise terms $S_{\ell m}(\vec{k})$ are given by

$$S_{\ell m}(\vec{k}) = \frac{C_{\text{shot}}(\vec{k})}{W_{\text{mass}}^2(\vec{k})} \left(\sum_i^{N_{\text{gal}}} + \alpha^2 \sum_i^{N_{\text{ran}}} \right) [w(\vec{x}_i)]^2 y_{\ell m}^*(\vec{x}_i). \quad (46)$$

The pair-counting approach has an advantage in a robust estimation of the correlation function at small scales compared to the FFT-based approach. On the other hand, the FFT-based approach is faster than pair-counting algorithms to calculate the correlation function. In this work, we adopt the FFT-based approach, because we use information on galaxy clustering at large scales, $40 h^{-1} \text{Mpc} < r$, in our analysis (for details, see Section 7.1).

The correlation function is not usually normalized by the factor A but the number of pairs of a random distribution at each bin r (Landy & Szalay 1993). Therefore, we finally present the following estimators of the spherical harmonic and BipoSH coefficients of the correlation function

$$\begin{aligned} \widehat{\xi}_{\ell m; \ell' m'}(r) &= \frac{\widehat{\xi}_{\ell m; \ell' m'}(r)|_A}{RR(r)}, \\ \widehat{\xi}_{\ell\ell'}^{LM}(r) &= \frac{\widehat{\xi}_{\ell\ell'}^{LM}(r)|_A}{RR(r)}, \end{aligned} \quad (47)$$

where $RR(r)$ is the auto-correlation function measured from

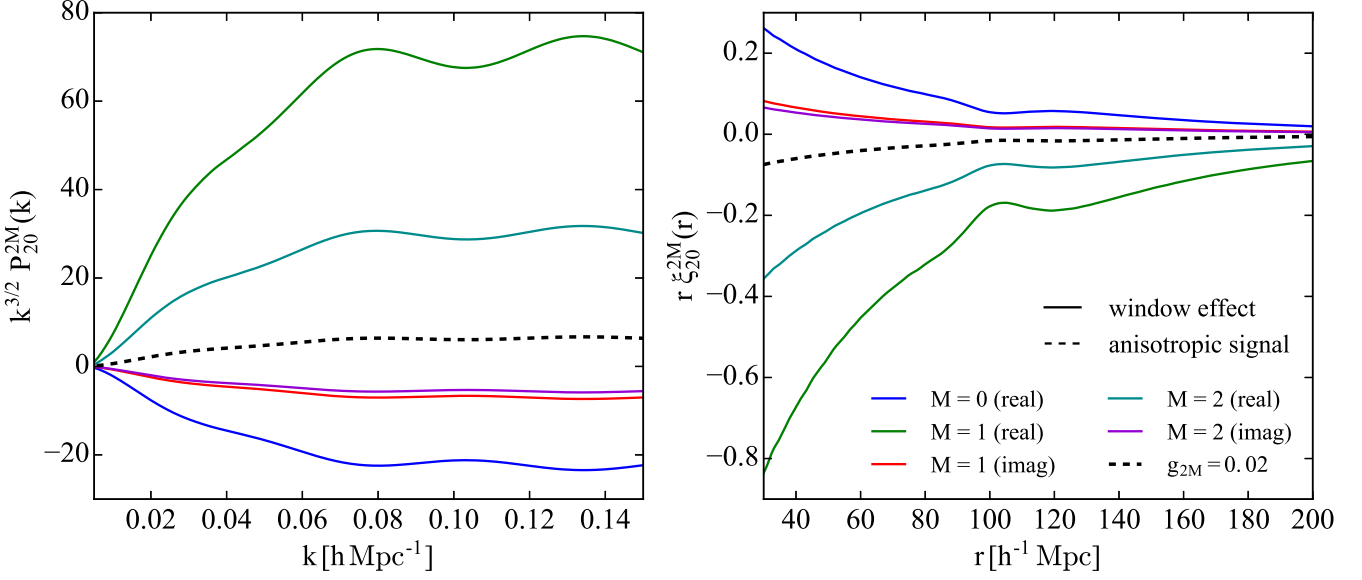


Figure 2. BipoSH coefficients of the power spectrum P_{20}^{2M} (left) and the correlation function ξ_{20}^{2M} (right) for CMASS NGC as given in equations (60) and (61), respectively. The solid colored lines represent the window function corrections, while the dashed black lines denote the primordial anisotropic signal. This figure shows that the mimic anisotropic signals induced by the survey geometry make a significant contribution to the observed BipoSH coefficients.

the random catalog

$$\begin{aligned} RR(r) &= \frac{1}{A} \int \frac{d^2 \hat{r}}{4\pi} \int d^3 x_1 \int d^3 x_2 \delta_D(\vec{r} - \vec{x}_{12}) \bar{n}(\vec{x}_1) \bar{n}(\vec{x}_2) \\ &= \frac{\alpha^2}{4\pi r^2 \Delta r A} \sum_{i,j}^{N_{\text{ran}}} \delta_K(r - |\vec{x}_{ij}|) w(\vec{x}_i) w(\vec{x}_j). \end{aligned} \quad (48)$$

The above estimators, $\widehat{\xi}_{\ell\ell'}^{LM}$ and $\widehat{\xi}_{\ell m; \ell' m'}$, are related to the Legendre coefficients estimator as follows

$$\widehat{\xi}_\ell(r) = \widehat{\xi}_{\ell\ell}^{00}(r) = \frac{1}{2\ell + 1} \sum_{m=-\ell}^{\ell} (-1)^m \widehat{\xi}_{\ell, -m; \ell m}(r). \quad (49)$$

5 SURVEY WINDOW FUNCTIONS

In this section, we discuss the effects of survey geometry asymmetries on our statistics, the BipoSH coefficients. A treatment of the survey geometry effects for the Legendre coefficients was recently developed by Wilson et al. (2015), based on configuration-space calculations. We extend their treatment to the BipoSH coefficients. In this section we present the main equations, leaving their full derivations in Appendix B.

The theoretical expression of the observed density fluctuation δn (equation 27) is described as

$$\delta n(\vec{x}) = \bar{n}(\vec{x}) (\delta(\vec{x}) - \bar{\delta}), \quad (50)$$

where $\delta(\vec{x})$ is the theoretically-predicted density perturbation, and the mean density perturbation $\bar{\delta}$ is given by

$$\bar{\delta} = \frac{1}{N_{\text{wg}}} \int d^3 x \bar{n}(\vec{x}) \delta(\vec{x}) \quad (51)$$

with N_{wg} being the weighted total number of galaxies $N_{\text{wg}} = \int d^3 x \bar{n}(\vec{x}) = \sum_i^{N_{\text{gal}}} w(\vec{x}_i)$. As the mean number density $\bar{n}(\vec{x})$ is estimated from a random distribution in a finite

survey volume, which is given by equation (26), it behaves as the survey mask. The mean density perturbation $\bar{\delta}$, the so-called integral constraint (Peacock & Nicholson 1991), comes from the difference between the measured mean density from a finite survey volume and the true value. Equation (50) satisfies $\int d^3 x \delta n(\vec{x}) = \delta n(\vec{k} = 0) = 0$ due to the integral constraint term. Using equation (50), we obtain

$$\langle \delta n(\vec{x}_1) \delta n(\vec{x}_2) \rangle = \bar{n}(\vec{x}_1) \bar{n}(\vec{x}_2) [\xi(\vec{x}_{12}, \hat{x}_1) - \langle \delta^2 \rangle], \quad (52)$$

where we used an approximation $\langle \delta(\vec{x}) \bar{\delta} \rangle \approx \langle \delta^2 \rangle$ ⁵. In the above expression, we do not use the global LOS direction \hat{n} used in Section 2 but a local LOS direction, $\hat{x}_1 \approx \hat{x}_2$, under the local plane parallel approximation. For the correlation function, the BipoSH expansion derived in Section 2 holds true even if we replace \hat{n} by \hat{x}_1 .⁶

Since we observe the BipoSH coefficients estimators, $\widehat{P}_{\ell\ell'}^{2M}(k)$ and $\widehat{\xi}_{\ell\ell'}^{2M}(r)$, given in Section 4, we should compute the ensemble averages of them, $\langle \widehat{P}_{\ell\ell'}^{2M}(k) \rangle$ and $\langle \widehat{\xi}_{\ell\ell'}^{2M}(r) \rangle$, to construct theoretical models for the BipoSH coefficients including the survey geometry effect. For that purpose, we first compute the ensemble average of $\widehat{\xi}_{\ell\ell'}^{LM}(r)|_A$ (equation 41):

$$\begin{aligned} \langle \widehat{\xi}_{\ell\ell'}^{LM}(r)|_A \rangle &= \frac{(2L+1)(2\ell+1)(2\ell'+1)H_{\ell\ell'}^L}{A} \int \frac{d^2 \hat{r}}{4\pi} \\ &\times \int d^3 x_1 \int d^3 x_2 \delta_D(\vec{r} - \vec{x}_{12}) S_{\ell\ell'}^{LM*}(\hat{r}, \hat{x}_1) \\ &\times \bar{n}(\vec{x}_1) \bar{n}(\vec{x}_2) [\xi(\vec{r}, \hat{x}_1) - \langle \delta^2 \rangle], \end{aligned} \quad (53)$$

where $\xi(\vec{r}, \hat{x}_1)$ can be expanded in BipoSHs (equation 15).

⁵ The treatment which does not rely on this approximation may be useful to improve the accuracy, but we leave it for future work.

⁶ The discussion in this section will hold true even if we do not use a local LOS direction \hat{x}_1 but the other definition of the LOS direction, e.g. the unit vector \hat{n}_{12} of $\vec{n}_{12} = (\vec{x}_1 + \vec{x}_2)/2$.

Second, we define the BipoSH coefficients of survey window functions as

$$Q_{\ell\ell'}^{LM}(r) \equiv (2L+1) H_{\ell\ell'}^L(-1)^M \times \sum_{mm'} \binom{\ell \ \ell' \ L}{m \ m' \ -M} Q_{\ell m; \ell' m'}(r), \quad (54)$$

where the spherical harmonic coefficients of the window function are given by

$$Q_{\ell m; \ell' m'}(r) = \frac{(2\ell+1)(2\ell'+1)}{A} \int \frac{d^2\hat{r}}{4\pi} y_{\ell m}^*(\hat{r}) \int d^3x_1 \int d^3x_2 \times \delta_D(\vec{r} - \vec{x}_{12}) y_{\ell' m'}^*(\hat{x}_1) \bar{n}(\vec{x}_1) \bar{n}(\vec{x}_2). \quad (55)$$

These spherical harmonic and BipoSH coefficients are related to the Legendre coefficients as follows

$$Q_\ell(r) = Q_{\ell\ell}^{00}(r) = \frac{1}{2\ell+1} \sum_{m=-\ell}^{\ell} (-1)^m Q_{\ell, -m; \ell m}(r), \quad (56)$$

where the monopole $Q_0(r)$ is equivalent to the function $RR(r)$ given by equation (48). Third, we compute the integral constraint term $\langle \bar{\delta}^2 \rangle$ (Appendix B1)

$$\langle \bar{\delta}^2 \rangle = \frac{4\pi}{V} \int dr r^2 \left[\sum_{\ell} \frac{1}{2\ell+1} Q_\ell(r) \xi_\ell(r) \right], \quad (57)$$

where the survey volume V is estimated as N_{wg}^2/A . Fourth, by substituting equations (15) and (54) into equation (53), we derive a linear combination of the correlation function and the window function, especially for $\langle \hat{\xi}_{20}^{2M} |_{\text{A}} \rangle$ (Appendix B2)

$$\begin{aligned} \langle \hat{\xi}_{20}^{2M}(r) |_{\text{A}} \rangle &= Q_0(r) \xi_{20}^{2M}(r) + Q_{20}^{2M}(r) [\xi_0(r) - \langle \bar{\delta}^2 \rangle] \\ &+ \frac{1}{5} [Q_{02}^{2M}(r) + Q_{22}^{2M}(r) + Q_{42}^{2M}(r)] \xi_2(r) \\ &+ \frac{1}{9} [Q_{24}^{2M}(r) + Q_{44}^{2M}(r)] \xi_4(r) \\ &+ \dots, \end{aligned} \quad (58)$$

where the first term corresponds to the signal of the statistical anisotropy, and the other terms arise from the survey geometry anisotropy. While we only use linear theory in our analysis, non-linear theories will yield additional higher Legendre coefficients other than the above expression, namely $\xi_{\ell \geq 6}$. Fifth, by keeping the dominant terms in equation (58), we have

$$\langle \hat{\xi}_{20}^{2M}(r) |_{\text{A}} \rangle \approx Q_0(r) \xi_{20}^{2M}(r) + \frac{1}{5} Q_{02}^{2M}(r) \xi_2(r). \quad (59)$$

We have checked and confirmed that the relative difference between equations (58) and (59) is within 10% on the scales of interest, $40 h^{-1} \text{Mpc} < r < 200 h^{-1} \text{Mpc}$. Since the errors in the observed BipoSH coefficients estimated from the BOSS data in Section 6.2 are significantly larger than this relative difference, this approximation will yield negligibly small changes in the final results. Finally, we derive the masked power spectrum from equation (43),

$$\begin{aligned} \langle \hat{P}_{20}^{2M}(k) \rangle &= -4\pi \int dr r^2 j_2(kr) \\ &\times \left[Q_0(r) \xi_{20}^{2M}(r) + \frac{1}{5} Q_{02}^{2M}(r) \xi_2(r) \right] \end{aligned} \quad (60)$$

and the masked correlation function from equation (47),

$$\langle \hat{\xi}_{20}^{2M}(r) \rangle = \xi_{20}^{2M}(r) + \frac{1}{5} \frac{Q_{02}^{2M}(r)}{Q_0(r)} \xi_2(r). \quad (61)$$

We use these equations (60) and (61) as a template model to fit the measurements of \hat{P}_{20}^{2M} and $\hat{\xi}_{20}^{2M}$ in Section 7. The theoretical predictions of ξ_{20}^{2M} and $\xi_{\ell=0,2}$ are given by equations (22) and (17), where the linear matter power spectrum used in this paper is generated with *CLASS* (Lesgourgues 2011).

Figure 1 shows the BipoSH coefficients of the survey window functions Q_{02}^{2M} for all M used in our analysis for CMASS NGC. They should be zero at larger scales than the survey volume ($\sim 1 h^{-1} \text{Gpc}$), while on small scales where the survey edge effects no longer matter, they become constant. These properties are similar to the monopole of the window function Q_0 (see e.g. Figure 2 in Beutler et al. (2016)).

Figure 2 shows the BipoSH coefficients of the power spectrum P_{20}^{2M} (left panel) and correlation function ξ_{20}^{2M} (right panel) for CMASS NGC. The solid colored lines represent the mimic anisotropic signals caused by the survey geometry, which are given by the second terms of equations (60) and (61), while the dashed black lines denote the primordial anisotropic signal described by the first terms, where we adopt $g_{2M} = 0.02$ as a typical value. We find that the effects of survey geometry on the BipoSH coefficients appear even on small scales and make a significant contribution to the observed power spectrum and correlation function.

6 MEASUREMENTS

6.1 Power spectrum and correlation function

In our analysis, we compute the power spectrum and the correlation function using the Fast Fourier Transform in the West (FFTW)⁷. We define the Cartesian coordinates $\vec{x} = (x, y, z)$ with z being the axis toward the north pole and place the LOWZ and CMASS samples in a cuboid of dimensions (L_x, L_y, L_z) [$h^{-1} \text{Mpc}$], where $(L_x, L_y, L_z) = (2400, 4200, 2400)$ for CMASS NGC, $(2600, 3400, 2000)$ for CMASS SGC, $(2300, 4000, 2300)$ for LOWZ NGC, and $(2400, 3200, 1700)$ for LOWZ SGC. We then distribute the CMASS and LOWZ galaxies on the FFT grid using the TSC assignment function with a 512 grid on an axis. This corresponds to a grid-cell resolution of $\sim 5 h^{-1} \text{Mpc}$ for both CMASS and LOWZ.

To estimate numerical convergence errors in FFT computations, we measure the power spectrum and the correlation function for CMASS NGC with two FFT grids, 512 and 1024, on an axis. We then define a fractional quantity, the difference between the two power spectra/correlation functions divided by the standard deviation of the power spectrum/correlation function estimated with the 512 grid in Section 6.2. We have checked that on the scales of interests, $0.01 h \text{Mpc}^{-1} < k < 0.10 h \text{Mpc}^{-1}$ and $40 h^{-1} \text{Mpc} < r < 200 h^{-1} \text{Mpc}$, the fractional differences for the power spectrum and correlation function are within 2% and 20%, respectively. Since the correlation function that is computed by the FFT-based approach will cause larger systematic biases than those induced by the power spectrum, we adopt

⁷ <http://fftw.org>

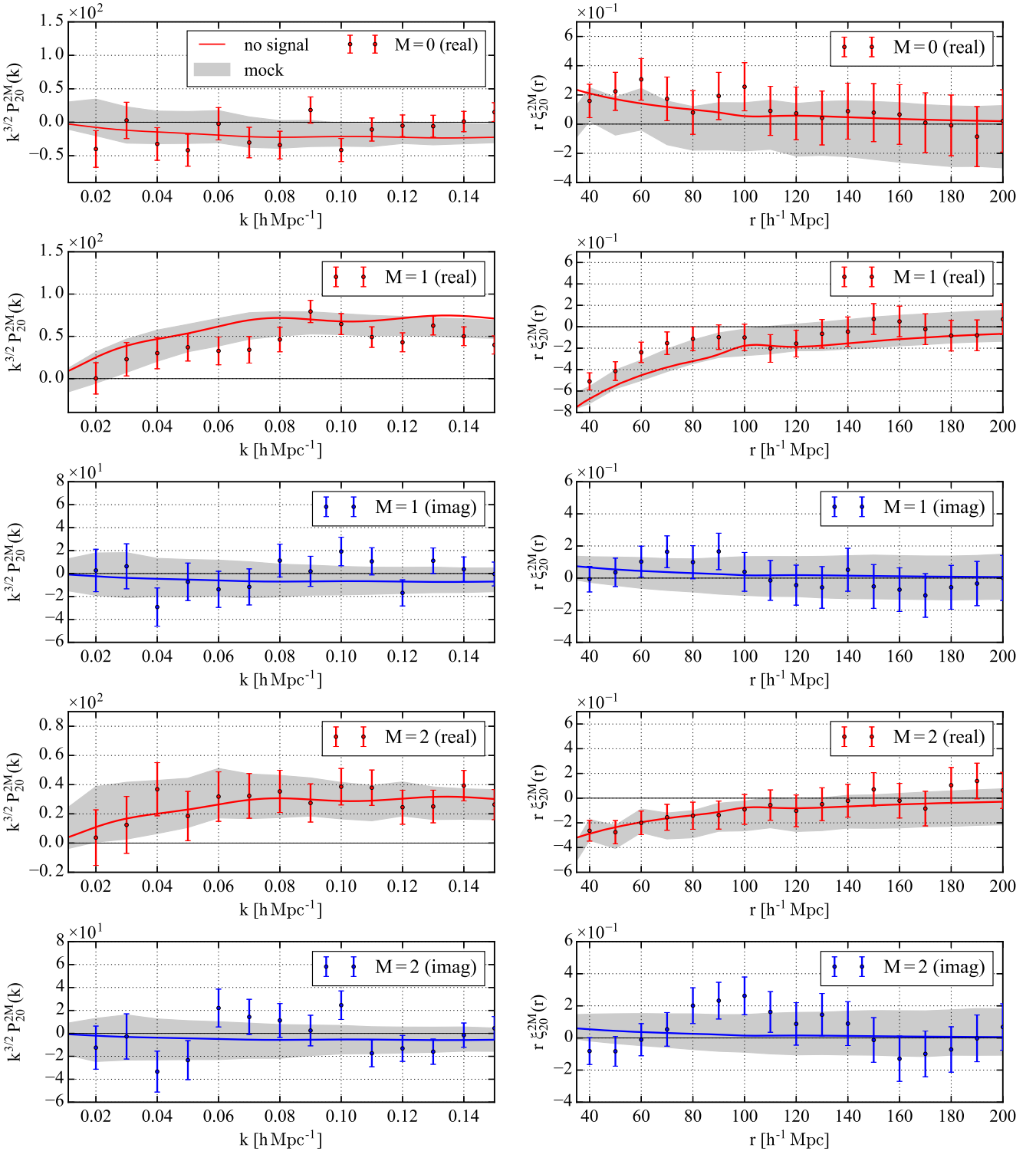


Figure 3. BipoSH coefficients of the power spectrum P_{20}^{2M} (left panels) and the correlation function ξ_{20}^{2M} (right panels) measured from CMASS NGC. The errorbars on the data points are derived from the 1σ errors measured from the QPM mocks. The gray shaded regions are the measurements from the QPM mocks, which do not include statistically anisotropic features, with the 1σ errors. The solid lines denote the predictions of the linear theory assuming no anisotropic signal, namely $g_{2M} = 0$, which are the same as the solid colored lines in Figure 2. The predictions from the QPM mocks and the theory only include the effects of survey geometry asymmetries and are in excellent agreement with the observations. Therefore, these figures show that the observed BipoSH coefficients, P_{20}^{2M} and ξ_{20}^{2M} for all M , can be sufficiently explained by the survey geometry effects.

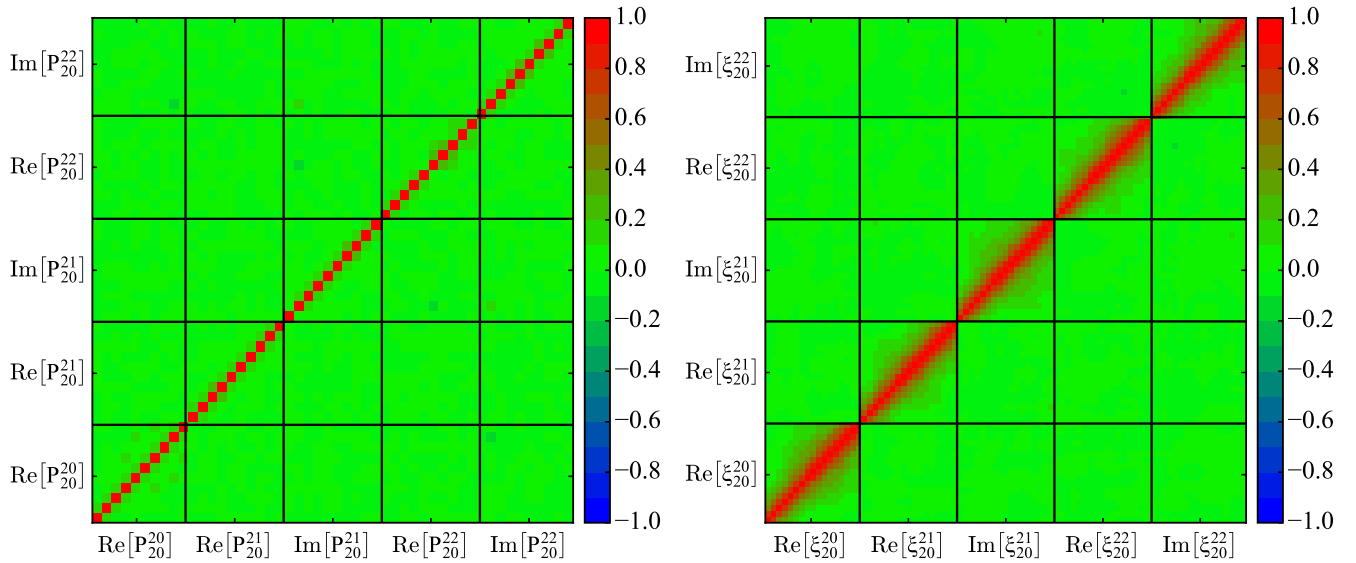


Figure 4. Correlation coefficient matrices of both the power spectrum (left) and the correlation function (right), estimated from the QPM mocks for CMASS NGC. In the left panel, each block separated by black lines includes k -bins between $k = 0.01\text{--}0.1 h \text{Mpc}^{-1}$, while in the right panel each block includes r -bins between $r = 40\text{--}200 h^{-1} \text{Mpc}$. The color indicates the level of correlation, where red represents high correlation, and green denotes low correlation. These figures indicate a very weak correlation between different two M modes of the BipoSH coefficients in both the Fourier- and configuration-space analyses.

the constraint on g_{2M} derived from the Fourier-space analysis as the main results.⁸

Figure 3 presents the measurements of both P_{20}^{2M} (left panels) and ξ_{20}^{2M} (right panels) for CMASS NGC using the estimators detailed in Sections 4.1 and 4.2, where their real and imaginary parts are shown by red and blue symbols, respectively. The solid lines are the fiducial models under the no anisotropic signal hypothesis $g_{2M} = 0$, which only include survey geometry corrections discussed in Section 5.

6.2 Covariance matrix

Once the power spectrum and correlation function are observed, it is necessary to estimate the error, namely the covariance matrix. One of the best ways to derive the covariance matrix is to utilize a number of mock catalogs made for a given sample. As shown in S17, the monopole of the power spectrum, P_0 , has a dominant contribution to the covariance matrix of the BipoSH coefficient P_{20}^{2M} . We thus expect that mock catalogs which do not include statistically anisotropic features are suited to use for the covariance estimate.

In this paper, we use the 999 Quick-Particle-Mesh (QPM) mock catalogs (White et al. 2014) that are based on low-resolution particle mesh simulations, in combination with the Halo Occupation Distribution (HOD) technique to populate the resolved halos with galaxies (see e.g. Tinker et al. (2012)). The QPM scheme incorporates observational effects including the survey selection window and fiber collisions. For the QPM mocks, the simu-

lation outputs are at $z = 0.55$ for CMASS and $z = 0.40$ for LOWZ. The fiducial cosmology for these mocks assumes a Λ CDM cosmology with $(\Omega_\Lambda, \Omega_m, \Omega_b, \sigma_8, h, n_s) = (0.71, 0.29, 0.0458, 0.80, 0.7, 0.97)$.

Using the QPM mocks, the covariance matrix for the statistic of interest y (either the power spectrum P or correlation function ξ) is given by

$$C_{ij} = \frac{1}{N_{\text{mock}} - 1} \sum_n^{N_{\text{mock}}} (y_i^n - \bar{y}_i)(y_j^n - \bar{y}_j), \quad (62)$$

where $N_{\text{mock}} = 999$, y_i^n is the i th binned value of the statistic y obtained from the n th mock, and \bar{y}_i is the mean value over the mocks, given by $\bar{y}_i = (1/N_{\text{mock}}) \sum_n^{N_{\text{mock}}} y_i^n$. We denote the power spectrum vector and the correlation function vector as $\vec{P} = \{\text{Re}[P_{20}^{20}], \text{Re}[P_{20}^{21}], \text{Im}[P_{20}^{21}], \text{Re}[P_{20}^{22}], \text{Im}[P_{20}^{22}]\}$ and $\vec{\xi} = \{\text{Re}[\xi_{20}^{20}], \text{Re}[\xi_{20}^{21}], \text{Im}[\xi_{20}^{21}], \text{Re}[\xi_{20}^{22}], \text{Im}[\xi_{20}^{22}]\}$, where each component of \vec{P} ($\vec{\xi}$) includes k -bins (r -bins). We then estimate the covariance matrices for the power spectrum and correlation function by replacing the vector \vec{y} in equation (62) by \vec{P} and $\vec{\xi}$, respectively. We only need the positive M modes of P_{20}^{2M} and ξ_{20}^{2M} due to the reality condition, $P_{20}^{2M*} = (-1)^M P_{20}^{2,-M}$ and $\xi_{20}^{2M*} = (-1)^M \xi_{20}^{2,-M}$.

The correlation coefficient matrix r_{ij} is defined as $r_{ij} = C_{ij}/(C_{ii}C_{jj})^{1/2}$. Figure 4 displays the correlation matrices of the power spectrum (left) and correlation function (right) for CMASS NGC. Each panel shows a matrix with five horizontal and vertical division lines that divide the matrix into 5×5 blocks. Each block in the left panel includes k -bins between $k = 0.01\text{--}0.1 h \text{Mpc}^{-1}$ with the bin width $\Delta k = 0.01 h \text{Mpc}^{-1}$, and each block in the right panel includes r -bins between $r = 40\text{--}200 h^{-1} \text{Mpc}$ with $\Delta r = 10 h^{-1} \text{Mpc}$. We observe that almost all elements in each off-diagonal block are less than 0.1 for the four samples, CMASS NGC, CMASS SGC, LOWZ NGC, and LOWZ

⁸ Although we use the power spectrum as the main analysis, the fractional difference of 20% for the correlation function will not significantly affect the constraint on the quadrupolar parameter, g_{2M} , due to larger error on g_{2M} than its signal, i.e. no evidence for violation of SI.

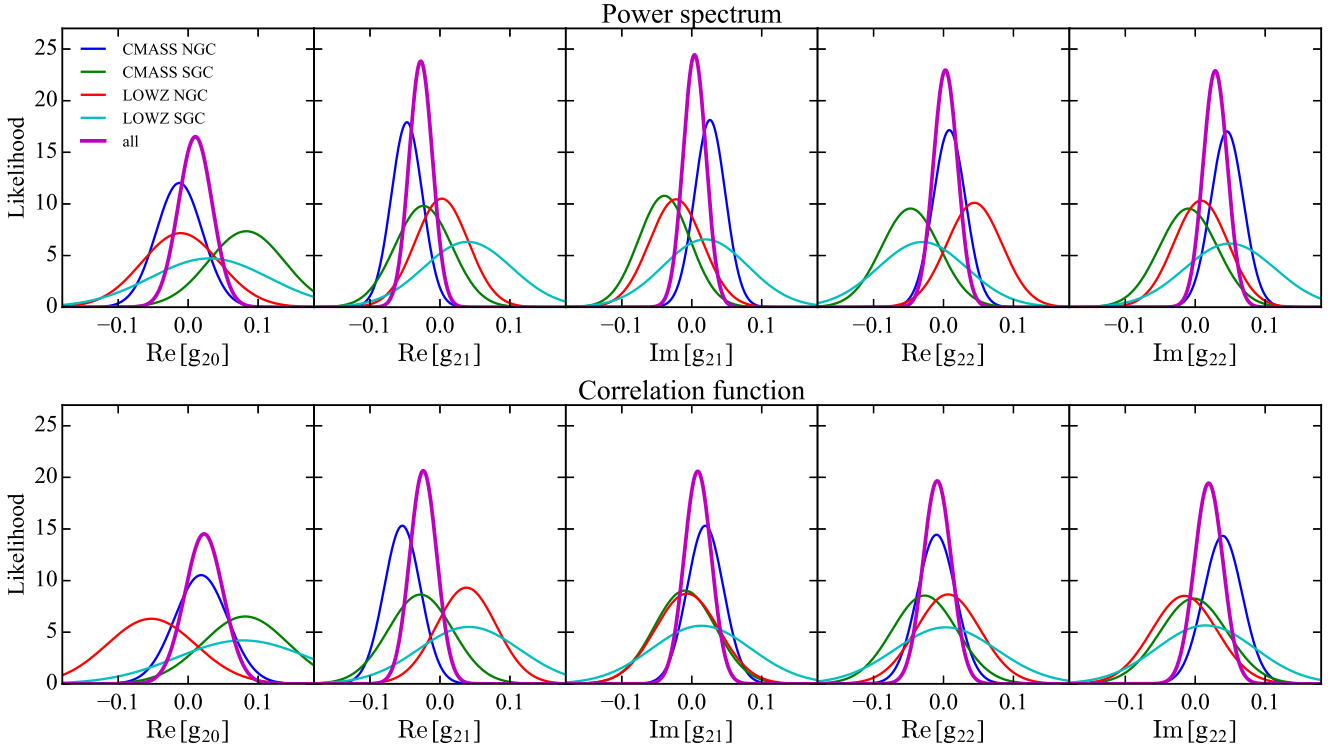


Figure 5. Likelihood functions for g_{2M} in Fourier (top panels) space and configuration (bottom panels) space. The colored lines in each panel show the likelihoods for four galaxy samples, CMASS NGC (blue), CMASS SGC (green), LOWZ NGC (red), and LOWZ SGC (cyan), and the likelihood computed by combining the four samples (purple). We treat the parameters g_{2M} for all M as statistically independent quantities and estimate the likelihoods for the four samples separately.

SGC, in both the Fourier- and configuration-space analyses. This fact indicates that there are negligibly small correlations between different two M modes of the BipoSH coefficients on the scales of interest in our analysis.

The error bars shown in Figure 3 are the standard deviation obtained by the square root of the diagonal components, $C_{ii}^{1/2}$. The gray shaded regions in Figure 3 are the measurements of P_{20}^{2M} and ξ_{20}^{2M} from the QPM mocks with the 1σ errors, which do not include the primordial anisotropic signal.

S17 has shown that there is no correlation between different M modes of the BipoSH coefficients in linear theory. This characteristic feature is consistent with the covariance estimate from the QPM mocks. In Appendix C, we compare the standard deviation (the square root of the diagonal elements of the covariance matrix) of P_{20}^{2M} computed by the linear theory developed in S17 with that estimated from the QPM mocks. We find an excellent agreement between the results from the theory and the mock, which validates both of the Fisher matrix computations performed by S17 and the error estimates in this paper.

As the estimated covariance matrix C_{ij} in Section 6.2 is inferred from a set of mocks, its inverse C_{ij}^{-1} is biased due to the limited number of realizations. We account for this effect by rescaling the inverse covariance matrix by the factor of equation (17) of Hartlap et al. (2007). We measure the standard χ^2 with this rescaled inverse covariance matrix. In addition to the Hartlap factor, we propagate the error in the covariance matrix to the error on g_{2M} by scaling the variance

for g_{2M} by the factor of equation (18) of Percival & et al. (2014).

7 ANALYSIS

7.1 Fitting prescription

We perform a standard likelihood analysis, where the likelihood function is computed as $L \propto \exp(-\chi^2/2)$ and the χ^2 -statistics is given by $\chi^2 = (\mathbf{d}^T - \mathbf{m}^T) \mathbf{C}^{-1} (\mathbf{d} - \mathbf{m})$ with the data vector \mathbf{d} , model vector \mathbf{m} , and covariance matrix \mathbf{C} . In our analysis, the data vector is the power spectrum vector \vec{P} or the correlation function vector $\vec{\xi}$, and the covariance matrix \mathbf{C} of each \vec{P} and $\vec{\xi}$ is given in Section 6.2. The model vector is computed by the ensemble average of the data vector, $\mathbf{m} = \langle \mathbf{d} \rangle$, as discussed in Section 5. We fit the BipoSH coefficients of the power spectrum, P_{20}^{2M} , and correlation function, ξ_{20}^{2M} , with the templates respectively given by equations (60) and (61) with the quadrupolar parameters g_{2M} for all M being free parameters. We fix the other parameters, the linear growth rate $f\sigma_8$, the linear bias $b\sigma_8$ and the cosmological parameters (see Section 1), using the Planck and BOSS results (Planck Collaboration et al. 2016a; Gil-Marín et al. 2016).

To determine the fitting ranges of the power spectrum and correlation function, we compute the χ^2 divided by the number of degrees of freedom (d.o.f), as a function of the maximum wavenumber k_{\max} in Fourier space and the minimum comoving distance r_{\min} in configuration space.

Power spectrum					
$g_{2M}/10^{-2}$	CMASS NGC	CMASS SGC	LOWZ NGC	LOWZ SGC	All
Re [g_{20}]	-0.81 ± 3.33	8.81 ± 5.44	-0.40 ± 5.58	4.00 ± 8.48	1.57 ± 2.42
Re [g_{21}]	-4.78 ± 2.24	-2.29 ± 4.07	0.03 ± 3.82	4.19 ± 6.33	-2.79 ± 1.68
Im [g_{21}]	2.61 ± 2.21	-3.95 ± 3.71	-2.24 ± 3.84	1.98 ± 6.10	0.40 ± 1.64
Re [g_{22}]	1.16 ± 2.33	-4.62 ± 4.19	4.87 ± 3.97	-2.88 ± 6.34	0.57 ± 1.74
Im [g_{22}]	4.51 ± 2.35	-1.04 ± 4.19	0.78 ± 3.88	4.93 ± 6.50	2.82 ± 1.74
Correlation function					
$g_{2M}/10^{-2}$	CMASS NGC	CMASS SGC	LOWZ NGC	LOWZ SGC	All
Re [g_{20}]	2.11 ± 3.81	9.06 ± 6.30	-4.93 ± 6.37	8.21 ± 9.55	2.65 ± 2.78
Re [g_{21}]	-5.44 ± 2.62	-3.00 ± 4.64	3.71 ± 4.31	4.24 ± 7.28	-2.46 ± 1.94
Im [g_{21}]	1.94 ± 2.62	-0.79 ± 4.36	-0.70 ± 4.60	1.38 ± 7.14	0.88 ± 1.94
Re [g_{22}]	-0.79 ± 2.78	-2.79 ± 4.83	0.94 ± 4.64	0.41 ± 7.34	-0.72 ± 2.05
Im [g_{22}]	3.91 ± 2.80	-0.37 ± 4.67	-1.62 ± 4.72	1.50 ± 7.10	1.84 ± 2.05

Table 1. Mean values of g_{2M} with their standard deviations. The upper and lower tables are for the Fourier- and configuration-space analyses, respectively. From second to fifth columns, the constraints on g_{2M} are given for four galaxy samples, CMASS-NGC, CMASS-SGC, LOWZ-NGC, and LOWZ-SGC. The sixth column presents the results obtained by combining all the samples, showing that the quadrupolar parameters g_{2M} for all M are of zero within the 2σ confidence level.

	CMASS NGC	CMASS SGC	LOWZ NGC	LOWZ SGC	All
Power Spectrum	$-0.14 < g_* < 0.09$	$-0.14 < g_* < 0.18$	$-0.12 < g_* < 0.11$	$-0.18 < g_* < 0.19$	$-0.093 < g_* < 0.079$
Correlation function	$-0.14 < g_* < 0.10$	$-0.13 < g_* < 0.18$	$-0.16 < g_* < 0.13$	$-0.19 < g_* < 0.23$	$-0.088 < g_* < 0.085$

Table 2. Limits on g_* with a 95% confidence level after marginalizing over the preferred direction \hat{p} .

We fix the minimum wavenumber $k_{\min} = 0.01 h \text{ Mpc}^{-1}$ and the maximum comoving distance $r_{\max} = 200 h^{-1} \text{ Mpc}$. We calculate the χ^2 using the QPM mocks and the model with $g_{2M} = 0$, clarifying the scales where the linear theory approximation breaks in our analysis. We find that $\chi^2/\text{d.o.f.}$ starts to significantly depart from unity at $k_{\max} \sim 0.1 h \text{ Mpc}^{-1}$ and $r_{\min} \sim 40 h^{-1} \text{ Mpc}$ for all the four galaxy samples. Therefore, we decide to use the fitting ranges of $k = 0.01 - 0.1 h \text{ Mpc}^{-1}$ and $r = 40 - 200 h \text{ Mpc}^{-1}$ and bin the power spectrum and correlation function in bins of $\Delta k = 0.01 h \text{ Mpc}^{-1}$ and $\Delta r = 10 h^{-1} \text{ Mpc}$.

Since the correlation between different M modes of each of P_{20}^{2M} and ξ_{20}^{2M} was shown to be very weak in Section 6.2, we treat the M modes of each P_{20}^{2M} and ξ_{20}^{2M} as statistically independent quantities in our analysis. This treatment implies that the quadrupolar parameters g_{2M} for all M are statistically independent of each other. To validate this treatment, we perform a full analysis for CMASS NGC in Fourier space. Namely, we compute the likelihood function for g_{2M} using the full covariance matrix of P_{20}^{2M} including the correlation between their different M modes and estimate the correlation coefficient matrix of g_{2M} . We then find that all off-diagonal elements of the correlation matrix of g_{2M} are less than 0.06, indicating no correlation between g_{2M} and $g_{2M'}$ for $M \neq M'$. We expect the similar results even for the other samples and for the configuration-space analysis.

7.2 Parameter constraints

Figure 5 shows the likelihood functions of g_{2M} for four galaxy samples, CMASS NGC (blue), CMASS SGC (green), LOWZ NGC (red), and LOWZ SGC (cyan), and the likelihood computed by combining these four samples (purple). We estimate the likelihood functions for the four samples separately, i.e. treat them as statistically independent samples. The top and bottom panels are the results for the power spectrum and correlation function, respectively. Since the quadrupolar parameter g_{2M} is a proportionality constant in our template model, the shape of each likelihood becomes closely similar to a Gaussian distribution. Table 1 presents the mean values of g_{2M} with their standard deviations σ_{2M} , which are computed from the corresponding likelihood functions with the flat priors, $-1 \leq \text{Re}[g_{2M}] \leq 1$ and $-1 \leq \text{Im}[g_{2M}] \leq 1$. For all the four samples, g_{2M} is consistent with zero at the 2σ level, except for $\text{Re}[g_{21}]$ for CMASS NGC. Combining all the samples, g_{2M} for all M are within 2σ of zero. We see consistency between the results from the Fourier- and configuration-space analyses.

Also of interest is a quadrupolar directional dependence of the primordial power spectrum, which is related to g_{2M} as (see e.g. equation 172 in Planck Collaboration et al. (2016c))

$$g_{2M} = \frac{8\pi}{15} g_* Y_{2M}^*(\hat{p}), \quad (63)$$

where \hat{p} is a preferred direction in space, and g_* is a parameter characterizing the amplitude of the anisotropy. Using

constraints on g_{2M} , the likelihood for g_* is given by

$$L(g_*) \propto \int d^2\hat{p} \exp\left(-\frac{1}{2} \sum_M \left(\frac{g_{2M} - \frac{8\pi}{15} g_* Y_{2M}^*(\hat{p})}{\sigma_{2M}}\right)^2\right), \quad (64)$$

where we marginalize over all possible directions of \hat{p} . Since we find that the shape of this likelihood is deviated from a Gaussian distribution, we compute the lower and upper limits on g_* with a 95% confidence level (CL) using the flat prior $-1 \leq g_* \leq 1$. We summarize the results in Table 2; combining all the four galaxy samples, our limit on g_* is $-0.09 < g_* < 0.08$ (95% CL). We also find that the marginalized likelihood for \hat{p} has many peaks, indicating no preferred direction in the Universe. This fact is consistent with the limit on g_* , i.e. no evidence of departures from SI.

7.3 Comparison with previous works

We end this paper by summarizing results of previous works and comparing them with our limits. The Planck CMB temperature maps provide the most stringent constraints on the anisotropy parameters, g_{2M} and g_* , to date: e.g., the 1σ errors on g_{20} and g_* are $\Delta g_{20} = 1.2 \times 10^{-2}$ (Planck Collaboration et al. 2016b) and $\Delta g_* = 0.016$ (Kim & Komatsu 2013). The limit on g_* from SDSS DR7 photometric galaxy data is $-0.41 < g_* < +0.38$ with a 95% confidence level (Pullen & Hirata 2010). Comparing with our results ($\Delta g_{20} = 2.4 \times 10^{-2}$ in Table 1 and $-0.09 < g_* < 0.08$ in Table 2), we conclude that our limits are about two times as weak as the limits provided by Planck, while this work does improve upon the constraints about four times as stringent as those from the SDSS DR7 photometric galaxy data.

8 CONCLUSIONS

Statistical isotropy is a key feature of the standard inflation theory and needs to be tested in various experiments. For this purpose, we apply the BipoSH decomposition technique to the galaxy power spectrum and correlation function. The BipoSH formalism allows us to parameterize departures from statistical isotropy regarding the total angular momentum L , and the presence of statistical anisotropy produces the $L \geq 1$ modes in the BipoSH coefficients. In this work, we focus especially on the quadrupolar-type anisotropy, which is associated with the $L = 2$ mode, and constrain the well-known quadrupolar anisotropy parameters, g_{2M} and g_* with the BipoSH coefficients extracted from the BOSS DR12 sample.

Survey geometry asymmetries potentially cause the largest systematic difference between the observed BipoSH coefficients and the intrinsic cosmological signal that we want to know. This work presents a modeling approach for predicting the BipoSH coefficients of the galaxy power spectrum and correlation function in light of the survey geometry effects. Figure 3 shows that the anisotropic signal due to the specific survey geometry provides a sufficient explanation of the observed BipoSH coefficients in the BOSS DR12 data, implying the statistical isotropy of the Universe.

Tables 1 and 2 summarize our constraints on the quadrupolar parameters, g_{2M} and g_* . Combining four

galaxy samples, CMASS NGC, CMASS SGC, LOWZ NGC, and LOWZ SGC, we find g_{2M} for all M to be of zero within the 2σ level and $-0.09 < g_* < 0.08$ with a 95% confidence level. The spectroscopic catalogs of BOSS thus provide an improvement by a factor of about four compared with the photometric catalogs of SDSS (Abazajian et al. 2009), $-0.4 < g_* < 0.38$ (95% CL) obtained by Pullen & Hirata (2010). These results are the best constraint on the quadrupolar parameter from galaxy survey data currently, while they are still weaker than the Planck results (Planck Collaboration et al. 2016b,c).

While we only use the linear regions, $k \leq 0.1 h \text{ Mpc}^{-1}$, in our analysis, non-linear information up to e.g. $k = 0.2 h \text{ Mpc}^{-1}$ could further shrink the errors on g_{2M} and g_* by a factor of two (Shiraishi et al. 2017). To do so, we will need the additional modeling of non-linear perturbation theories and fiber collisions on small scales.

The tools and techniques that we have discussed here may be straightforwardly applied to constraining any source of statistical anisotropy, e.g. tidal forces τ_{ij} arising from the super-sample mode beyond the survey area (Akitsu et al. 2016). The BOSS data will provide the same order of errors on τ_{ij} as that associated with the quadrupolar parameter, namely $\Delta\tau_{ij} = \mathcal{O}(10^{-2})$.

All the analysis presented in this work will be directly applicable to future spectroscopic galaxy surveys, e.g. the Subaru Prime Focus Spectrograph (PFS; Takada et al. (2014)), the Dark Energy Spectroscopic Instrument (DESI; Levi et al. (2013)), and Euclid (Laureijs et al. 2011), which will provide much better sensitivity to g_{2M} and g_* . We have forecast in Shiraishi et al. (2017) that PFS and Euclid could achieve the sensitivity comparable to or even better than the Planck results (Planck Collaboration et al. 2016b,c).

ACKNOWLEDGEMENTS

We are grateful to Yin Li for discussion. NSS and MS acknowledge financial support from Grant-in-Aid for JSPS Fellows (Nos. 28-1890 and 27-10917). We were supported in part by the World Premier International Research Center Initiative (WPI Initiative), MEXT, Japan. Numerical computations were carried out on Cray XC30 at Center for Computational Astrophysics, National Astronomical Observatory of Japan.

Funding for SDSS-III has been provided by the Alfred P. Sloan Foundation, the Participating Institutions, the National Science Foundation, and the U.S. Department of Energy Office of Science. The SDSS-III web site is <http://www.sdss3.org/>. SDSS-III is managed by the Astrophysical Research Consortium for the Participating Institutions of the SDSS-III Collaboration including the University of Arizona, the Brazilian Participation Group, Brookhaven National Laboratory, Carnegie Mellon University, University of Florida, the French Participation Group, the German Participation Group, Harvard University, the Instituto de Astrofísica de Canarias, the Michigan State/Notre Dame/JINA Participation Group, Johns Hopkins University, Lawrence Berkeley National Laboratory, Max Planck Institute for Astrophysics, Max Planck Institute for Extraterrestrial Physics, New Mexico State University, New

York University, Ohio State University, Pennsylvania State University, University of Portsmouth, Princeton University, the Spanish Participation Group, University of Tokyo, University of Utah, Vanderbilt University, University of Virginia, University of Washington, and Yale University.

REFERENCES

- Abazajian K. N., et al., 2009, *Astrophys. J. Suppl.*, 182, 543
 Ackerman L., Carroll S. M., Wise M. B., 2007, *Phys. Rev. D*, 75, 083502
 Akitsu K., Takada M., Li Y., 2016
 Alam S., et al., 2015, *ApJS*, 219, 12
 Alam S., et al., 2016, Submitted to: *Mon. Not. Roy. Astron. Soc.*
 Albrecht A., Steinhardt P. J., 1982, *Phys. Rev. Lett.*, 48, 1220
 Anderson L., et al., 2014, *MNRAS*, 441, 24
 Ashoorioon A., Casadio R., Koivisto T., 2016, *JCAP*, 1612, 002
 Bartolo N., Dimastrogiovanni E., Matarrese S., Riotto A., 2009a, *J. Cosmology Astropart. Phys.*, 10, 015
 Bartolo N., Dimastrogiovanni E., Matarrese S., Riotto A., 2009b, *J. Cosmology Astropart. Phys.*, 11, 028
 Bartolo N., Matarrese S., Peloso M., Ricciardone A., 2013a, *Phys. Rev. D*, 87, 023504
 Bartolo N., Matarrese S., Peloso M., Ricciardone A., 2013b, *JCAP*, 1308, 022
 Bartolo N., Peloso M., Ricciardone A., Unal C., 2014, *JCAP*, 1411, 009
 Bartolo N., Matarrese S., Peloso M., Shiraishi M., 2015a, *J. Cosmology Astropart. Phys.*, 1, 027
 Bartolo N., Matarrese S., Peloso M., Shiraishi M., 2015b, *J. Cosmology Astropart. Phys.*, 7, 039
 Bennett C. L., et al., 1996, *Astrophys. J.*, 464, L1
 Bennett C. L., et al., 2011, *ApJS*, 192, 17
 Bennett C. L., et al., 2013, *ApJS*, 208, 20
 Beutler F., et al., 2016, preprint, ([arXiv:1607.03150](https://arxiv.org/abs/1607.03150))
 Bianchi D., Gil-Marín H., Ruggeri R., Percival W. J., 2015, *MNRAS*, 453, L11
 Bolton A. S., et al., 2012, *AJ*, 144, 144
 Bundy K., et al., 2015, *ApJS*, 221, 15
 Dawson K. S., et al., 2013, *AJ*, 145, 10
 Dimopoulos K., 2006, *Phys. Rev. D*, 74, 083502
 Dimopoulos K., Karčiauskas M., 2008, *Journal of High Energy Physics*, 7, 119
 Dimopoulos K., Karčiauskas M., Wagstaff J. M., 2010, *Phys. Rev. D*, 81, 023522
 Doi M., et al., 2010, *AJ*, 139, 1628
 Eisenstein D. J., et al., 2005, *ApJ*, 633, 560
 Eisenstein D. J., et al., 2011, *AJ*, 142, 72
 Feldman H. A., Kaiser N., Peacock J. A., 1994, *ApJ*, 426, 23
 Fukugita M., Ichikawa T., Gunn J. E., Doi M., Shimasaku K., Schneider D. P., 1996, *AJ*, 111, 1748
 Gil-Marín H., et al., 2016, *MNRAS*, 460, 4188
 Groeneboom N. E., Eriksen H. K., 2009, *Astrophys. J.*, 690, 1807
 Groeneboom N. E., Ackerman L., Wehus I. K., Eriksen H. K., 2010, *Astrophys. J.*, 722, 452
 Gümrükçüoğlu A. E., Himmetoglu B., Peloso M., 2010, *Phys. Rev. D*, 81, 063528
 Gunn J. E., et al., 1998, *AJ*, 116, 3040
 Gunn J. E., et al., 2006, *AJ*, 131, 2332
 Guth A. H., 1981, *Phys. Rev.*, D23, 347
 Hajian A., Souradeep T., 2003, *Astrophys. J.*, 597, L5
 Hajian A., Souradeep T., 2006, *Phys. Rev.*, D74, 123521
 Hajian A., Souradeep T., Cornish N. J., 2004, *Astrophys. J.*, 618, L63
 Hamilton A. J. S., 1998, in Hamilton D., ed., *Astrophysics and Space Science Library* Vol. 231, The Evolving Universe. p. 185 ([arXiv:astro-ph/9708102](https://arxiv.org/abs/astro-ph/9708102)), [doi:10.1007/978-94-011-4960-0_17](https://doi.org/10.1007/978-94-011-4960-0_17)
 Hanson D., Lewis A., 2009, *Phys. Rev. D*, 80, 063004
 Hartlap J., Simon P., Schneider P., 2007, *A&A*, 464, 399
 Himmetoglu B., Contaldi C. R., Peloso M., 2009a, *Phys. Rev. D*, 80, 123530
 Himmetoglu B., Contaldi C. R., Peloso M., 2009b, *Physical Review Letters*, 102, 111301
 Hinshaw G., et al., 2013, *ApJS*, 208, 19
 Jing Y. P., 2005, *ApJ*, 620, 559
 Kaiser N., 1987, *MNRAS*, 227, 1
 Kim J., Komatsu E., 2013, *Phys. Rev. D*, 88, 101301
 Landy S. D., Szalay A. S., 1993, *ApJ*, 412, 64
 Laureijs R., et al., 2011
 Leauthaud A., et al., 2016, *MNRAS*, 457, 4021
 Lesgourgues J., 2011
 Levi M., et al., 2013, preprint, ([arXiv:1308.0847](https://arxiv.org/abs/1308.0847))
 Linde A. D., 1982, *Phys. Lett.*, B108, 389
 Naruko A., Komatsu E., Yamaguchi M., 2015, *J. Cosmology Astropart. Phys.*, 4, 045
 Parejko J. K., et al., 2013, *MNRAS*, 429, 98
 Peacock J. A., Nicholson D., 1991, *MNRAS*, 253, 307
 Percival W. J., et al. 2014, *MNRAS*, 439, 2531
 Planck Collaboration et al., 2016a, *A&A*, 594, A13
 Planck Collaboration et al., 2016b, *A&A*, 594, A16
 Planck Collaboration et al., 2016c, *A&A*, 594, A20
 Pullen A. R., Hirata C. M., 2010, *J. Cosmology Astropart. Phys.*, 5, 027
 Ramazanov S., Rubtsov G., Thorsrud M., Urban F. R., 2017, *JCAP*, 1703, 039
 Reid B., et al., 2016, *MNRAS*, 455, 1553
 Ross A. J., et al., 2012, *MNRAS*, 424, 564
 Saito S., et al., 2016, *MNRAS*, 460, 1457
 Samushia L., Branchini E., Percival W. J., 2015, *MNRAS*, 452, 3704
 Sato K., 1981, *Mon. Not. Roy. Astron. Soc.*, 195, 467
 Scoccimarro R., 2015, *Phys. Rev. D*, 92, 083532
 Shiraishi M., Sugiyama N. S., Okumura T., 2017, *Phys. Rev.*, D95, 063508
 Slepian Z., Eisenstein D. J., 2016, *Mon. Not. Roy. Astron. Soc.*, 455, L31
 Smith J. A., et al., 2002, *AJ*, 123, 2121
 Soda J., 2012, *Classical and Quantum Gravity*, 29, 083001
 Starobinsky A. A., 1980, *Phys. Lett.*, B91, 99
 Szapudi I., 2004, *ApJ*, 614, 51
 Takada M., et al., 2014, *PASJ*, 66, R1
 Tinker J. L., et al., 2012, *ApJ*, 745, 16
 Varshalovich D. A., Moskalev A. N., Khersonskii V. K., 1988, *Quantum Theory of Angular Momentum*. World Scientific Publishing Co, [doi:10.1142/0270](https://doi.org/10.1142/0270)
 Watanabe M., Kanno S., Soda J., 2010, *Progress of Theoretical Physics*, 123, 1041
 White M., et al., 2011, *ApJ*, 728, 126
 White M., Tinker J. L., McBride C. K., 2014, *MNRAS*, 437, 2594
 Wilson M. J., Peacock J. A., Taylor A. N., de la Torre S., 2015, preprint, ([arXiv:1511.07799](https://arxiv.org/abs/1511.07799))
 Yamamoto K., Nakamichi M., Kamino A., Bassett B. A., Nishioka H., 2006, *PASJ*, 58, 93
 Yokoyama S., Soda J., 2008, *J. Cosmology Astropart. Phys.*, 8, 005

APPENDIX A: SCALE-DEPENDENCE OF THE QUADRUPOLAR MODULATION

We consider the scale dependence of the quadrupolar modulation, namely $f(k) \neq 1$ in equation (18). We assume $f(k)$ as

a power law, $f(k) = (k/k_0)^n$ with three values of the spectral index, $n = -2, -1, \text{ and } 1$. Our constraints on g_{2M} and g_* will then depend on the pivot scale, chosen as $k_0 = 0.05 \text{ h Mpc}^{-1}$ as elsewhere (e.g., Planck Collaboration et al. (2016c)). Tables A1 and A2 show the constraints on g_{2M} and g_* , respectively.

APPENDIX B: DERIVATIONS OF EQUATIONS

B1 Derivation of equation (57)

The variance of the mean density perturbation $\bar{\delta}$ (equation 51) is given by

$$\begin{aligned} \langle \bar{\delta}^2 \rangle &= \frac{1}{N_{\text{wg}}^2} \int d^3 r \int d^3 x_1 \int d^3 x_2 \delta_{\text{D}}(\vec{r} - \vec{x}_{12}) \\ &\times \bar{n}(\vec{x}_1) \bar{n}(\vec{x}_2) \xi(\vec{r}, \hat{x}_1), \end{aligned} \quad (\text{B1})$$

where we used $\langle \delta(\vec{x}_1) \delta(\vec{x}_2) \rangle = \xi(\vec{x}_{12}, \hat{x}_1)$ with $\vec{x}_{12} = \vec{x}_1 - \vec{x}_2$. By expanding $\xi(\vec{r}, \hat{x}_1)$ in BipoSHs, we obtain

$$\begin{aligned} \langle \bar{\delta}^2 \rangle &= \frac{1}{N_{\text{wg}}^2} \int d^3 r \int d^3 x_1 \int d^3 x_2 \delta_{\text{D}}(\vec{r} - \vec{x}_{12}) \bar{n}(\vec{x}_1) \bar{n}(\vec{x}_2) \\ &\times \left[\sum_{\ell} \xi_{\ell}(r) \mathcal{L}_{\ell}(\hat{r} \cdot \hat{x}_1) + \xi_{\ell\ell'}^{LM}(r) \frac{S_{\ell\ell'}^{LM}(\hat{r}, \hat{x}_1)}{H_{\ell\ell'}^L} \right] \\ &= \frac{4\pi}{V} \int dr r^2 \left[\sum_{\ell} \frac{1}{2\ell+1} Q_{\ell}(r) \xi_{\ell}(r) \right] \\ &+ \frac{4\pi}{V} \sum_{L \geq 1} \sum_{\ell\ell'} \int dr r^2 \left[\frac{Q_{\ell\ell'}^{LM*}(r) \xi_{\ell\ell'}^{LM}(r)}{(2\ell+1)(2\ell'+1)(2L+1)(H_{\ell\ell'}^L)^2} \right] \end{aligned} \quad (\text{B2})$$

where the survey volume V is estimated as N_{wg}^2/A with A being the normalization factor given by equation (29). We ignore the statistically anisotropic terms $\xi_{\ell\ell'}^{L \geq 1, M}$, because they are clearly subdominant in the integral constraint, resulting in equation (57).

B2 Derivation of equation (58)

We start with equation (53) and expand the two-point correlation function $\xi(\vec{r}, \hat{x}_1)$ in BipoSHs:

$$\begin{aligned} \langle \hat{\xi}_{\ell\ell'}^{LM}(r) |_{\text{A}} \rangle &= \frac{(2\ell+1)(2\ell'+1)(2L+1)H_{\ell\ell'}^L}{A} \int \frac{d^2 \hat{r}}{4\pi} \int d^3 x_1 \int d^3 x_2 \\ &\times \delta_{\text{D}}(\vec{r} - \vec{x}_{12}) S_{\ell\ell'}^{LM*}(\hat{r}, \hat{x}_1) \bar{n}(\vec{x}_1) \bar{n}(\vec{x}_2) \\ &\times \left[\sum_{L_1 + \ell_1 + \ell'_1 = \text{even}, M_1} \xi_{\ell_1 \ell'_1}^{L_1 M_1}(r) \frac{S_{\ell_1 \ell'_1}^{L_1 M_1}(\hat{r}, \hat{x}_1)}{H_{\ell_1 \ell'_1}^{L_1}} \right], \end{aligned} \quad (\text{B3})$$

where we do not consider the integral constraint in the derivation, because the term simply yield $Q_{\ell\ell'}^{LM}(r) \langle \bar{\delta}^2 \rangle$. We use the relation

$$\begin{aligned} S_{\ell\ell'}^{LM*}(\hat{r}, \hat{n}) S_{\ell_1 \ell'_1}^{L_1 M_1}(\hat{r}, \hat{n}) &= \sum_{L_2 M_2} \sum_{\ell_2 \ell'_2} (2L_2+1)(2\ell_2+1)(2\ell'_2+1) \\ &\times T_{\ell\ell'; \ell_1 \ell'_1; \ell_2 \ell'_2}^{LM; L_1 M_1; L_2 M_2} S_{\ell_2 \ell'_2}^{L_2 M_2*}(\hat{k}, \hat{n}), \end{aligned} \quad (\text{B4})$$

where the coefficients T are given by

$$\begin{aligned} T_{\ell\ell'; \ell_1 \ell'_1; \ell_2 \ell'_2}^{LM; L_1 M_1; L_2 M_2} &= (-1)^M (-1)^{\ell + \ell' + L} H_{\ell_1 \ell_2}^{\ell} H_{\ell'_1 \ell'_2}^{\ell'} \\ &\times \begin{pmatrix} L & L_1 & L_2 \\ M & -M_1 & -M_2 \end{pmatrix} \left\{ \begin{matrix} L & L_1 & L_2 \\ \ell & \ell_1 & \ell_2 \\ \ell' & \ell'_1 & \ell'_2 \end{matrix} \right\}. \end{aligned} \quad (\text{B5})$$

We note here that if $\ell + \ell' + L = \text{even}$ and $\ell_1 + \ell'_1 + L_1 = \text{even}$, the coefficients T are zero for $\ell_2 + \ell'_2 + L_2 = \text{odd}$. We can then derive $\langle \hat{\xi}_{\ell\ell'}^{LM}(r) |_{\text{A}} \rangle$ for $\ell + \ell' + L = \text{even}$ as follows

$$\begin{aligned} \langle \hat{\xi}_{\ell\ell'}^{LM}(r) |_{\text{A}} \rangle &= \sum_{\ell_1 + \ell'_1 + L_1 = \text{even}} \sum_{\ell_2 + \ell'_2 + L_2 = \text{even}} \sum_{M_1 M_2} \\ &(2L+1)(2\ell+1)(2\ell'+1) T_{\ell\ell'; \ell_1 \ell'_1; \ell_2 \ell'_2}^{LM; L_1 M_1; L_2 M_2} \\ &\times \left(\frac{H_{\ell\ell'}^L}{H_{\ell_1 \ell'_1}^{L_1} H_{\ell_2 \ell'_2}^{L_2}} \right) Q_{\ell_2 \ell'_2}^{L_2 M_2}(r) \xi_{\ell_1 \ell'_1}^{L_1 M_1}(r). \end{aligned} \quad (\text{B6})$$

For $\langle \hat{\xi}_{20}^{2M}(r) |_{\text{A}} \rangle$, we obtain equation (58).

APPENDIX C: STANDARD DEVIATION

In linear theory, the covariance matrix of P_{20}^{2M} is given by (see equation (26) in Shiraishi et al. (2017))

$$\text{Cov} \left(P_{20}^{2M*}(k), P_{20}^{2M'}(k') \right) \simeq 10 \delta_{MM'} \delta_{kk'} \frac{1}{N_k} \left(P_0(k) + \frac{1}{\bar{n}_{\text{g}}} \right)^2, \quad (\text{C1})$$

where $N_k = 4\pi k^2 \Delta k V / (2\pi)^3$ is the number of independent Fourier modes in a bin with the survey volume V and the bin width Δk , P_0 is the monopole of the power spectrum, and \bar{n}_{g} is the galaxy mean number density. In the above expression, we ignore higher Legendre multipoles than the monopole because of their smallness. This equation shows that there is no correlation between different two M modes of P_{20}^{2M} , and that the covariance does not depend on the value of M .

Figure C1 compares the standard deviation of P_{20}^{2M} estimated from the QPM mocks for CMASS NGC in Section 6.2 (colored lines) with that computed by equation (C1) (black line). We estimate the survey volume and the mean number density for CMASS NGC as $V = 2.57 h^3 \text{ Gpc}^3$ and $\bar{n}_{\text{g}} = 2.57 \times 10^{-4} h^3 \text{ Mpc}^{-3}$, respectively. As expected, the standard deviations of P_{20}^{2M} for three M modes, $M = 0, 1, \text{ and } 2$, computed from the QPM mocks are closely similar to each other. We find an excellent agreement between the results from the linear theory and the QPM mocks until $k \sim 0.1 \text{ h Mpc}^{-1}$, while the linear approximation breaks on smaller scales than $k \sim 0.1 \text{ h Mpc}^{-1}$.

This paper has been typeset from a $\text{\TeX}/\text{\LaTeX}$ file prepared by the author.

Power spectrum						
Spectral index	$g_{2M}/10^{-2}$	CMASS NGC	CMASS SGC	LOWZ NGC	LOWZ SGC	All
$n = -2$	Re [g_{20}]	0.78 ± 2.01	6.02 ± 4.14	-2.24 ± 3.29	5.66 ± 6.54	1.11 ± 1.54
	Re [g_{21}]	-2.18 ± 1.39	3.04 ± 2.77	0.36 ± 2.30	3.01 ± 4.42	-0.57 ± 1.06
	Im [g_{21}]	-0.18 ± 1.37	0.87 ± 3.09	-1.59 ± 2.43	-2.92 ± 4.39	-0.50 ± 1.08
	Re [g_{22}]	-0.65 ± 1.40	2.89 ± 3.22	1.93 ± 2.46	2.99 ± 4.61	0.50 ± 1.11
	Im [g_{22}]	-1.17 ± 1.41	4.93 ± 2.98	-2.42 ± 2.43	-2.09 ± 4.51	-0.65 ± 1.09
$n = -1$	Re [g_{20}]	-0.79 ± 3.96	11.1 ± 6.86	-1.12 ± 6.77	9.04 ± 10.7	2.08 ± 2.94
	Re [g_{21}]	-6.67 ± 2.69	0.95 ± 5.06	0.43 ± 4.75	6.04 ± 7.99	-3.25 ± 2.05
	Im [g_{21}]	1.23 ± 2.68	-3.20 ± 4.78	-3.61 ± 4.61	-1.08 ± 7.57	-0.64 ± 2.01
	Re [g_{22}]	0.45 ± 2.81	-1.15 ± 5.40	5.31 ± 4.85	1.02 ± 7.99	1.18 ± 2.13
	Im [g_{22}]	1.73 ± 2.85	1.45 ± 5.22	-2.41 ± 4.72	2.27 ± 8.04	0.88 ± 2.13
$n = +1$	Re [g_{20}]	-0.38 ± 2.05	5.33 ± 3.36	-0.88 ± 3.44	1.15 ± 5.18	0.79 ± 1.49
	Re [g_{21}]	-2.22 ± 1.40	-2.22 ± 2.49	-0.27 ± 2.32	2.14 ± 3.76	-1.56 ± 1.06
	Im [g_{21}]	2.29 ± 1.37	-2.52 ± 2.27	-0.76 ± 2.37	1.87 ± 3.71	0.75 ± 1.01
	Re [g_{22}]	0.82 ± 1.45	-3.98 ± 2.55	3.07 ± 2.43	-2.89 ± 3.83	0.12 ± 1.07
	Im [g_{22}]	3.50 ± 1.44	-0.53 ± 2.54	1.38 ± 2.37	3.73 ± 3.98	2.37 ± 1.07

Correlation function						
Spectral index	$g_{2M}/10^{-2}$	CMASS NGC	CMASS SGC	LOWZ NGC	LOWZ SGC	All
$n = -2$	Re [g_{20}]	-0.43 ± 2.75	4.15 ± 5.07	-3.31 ± 4.69	11.1 ± 7.70	0.60 ± 2.07
	Re [g_{21}]	-3.67 ± 1.87	2.82 ± 3.44	-0.49 ± 3.41	2.41 ± 5.48	-1.59 ± 1.43
	Im [g_{21}]	0.35 ± 1.90	-0.33 ± 3.45	-2.09 ± 3.29	-1.91 ± 5.31	-0.39 ± 1.43
	Re [g_{22}]	-0.68 ± 1.93	1.97 ± 3.84	-0.66 ± 3.44	2.43 ± 5.63	-0.06 ± 1.49
	Im [g_{22}]	-0.77 ± 1.94	3.46 ± 3.52	-4.04 ± 3.35	-3.73 ± 5.63	-0.87 ± 1.47
$n = -1$	Re [g_{20}]	0.38 ± 4.24	9.34 ± 7.18	-4.15 ± 7.22	13.6 ± 11.1	2.28 ± 3.13
	Re [g_{21}]	-6.71 ± 2.90	0.34 ± 5.20	2.65 ± 5.04	5.55 ± 8.29	-2.86 ± 2.18
	Im [g_{21}]	1.10 ± 2.90	-1.39 ± 4.96	-2.80 ± 5.03	-0.56 ± 7.97	-0.21 ± 2.16
	Re [g_{22}]	-0.75 ± 3.05	-0.22 ± 5.52	0.42 ± 5.26	1.84 ± 8.42	-0.25 ± 2.29
	Im [g_{22}]	1.75 ± 3.10	1.49 ± 5.30	-3.58 ± 5.20	-0.49 ± 8.24	0.50 ± 2.28
$n = +1$	Re [g_{20}]	2.86 ± 2.86	7.17 ± 4.76	-4.36 ± 4.76	4.41 ± 7.06	2.44 ± 2.08
	Re [g_{21}]	-3.38 ± 1.99	-3.41 ± 3.50	3.28 ± 3.19	2.50 ± 5.33	-1.55 ± 1.46
	Im [g_{21}]	1.91 ± 2.02	0.08 ± 3.29	0.95 ± 3.47	1.44 ± 5.32	1.33 ± 1.48
	Re [g_{22}]	-0.91 ± 2.11	-3.20 ± 3.63	1.02 ± 3.44	0.41 ± 5.39	-0.83 ± 1.55
	Im [g_{22}]	3.34 ± 2.10	-0.28 ± 3.48	-0.44 ± 3.54	1.63 ± 5.18	1.78 ± 1.53

Table A1. Same as Table 1 except for the scale-dependence of the quadrupolar modulation, $f(k) = (k/k_0)^n$ with $n = -2, -1, \text{ and } 1$, where the pivot scale is chosen as $k_0 = 0.05 h \text{ Mpc}^{-1}$.

Power spectrum					
Spectral index	CMASS NGC	CMASS SGC	LOWZ NGC	LOWZ SGC	All
$n = -2$	$-0.05 < g_* < 0.05$	$-0.52 < g_* < 0.14$	$-0.08 < g_* < 0.08$	$-0.13 < g_* < 0.16$	$-0.040 < g_* < 0.044$
$n = -1$	$-0.13 < g_* < 0.11$	$-0.14 < g_* < 0.21$	$-0.15 < g_* < 0.14$	$-0.21 < g_* < 0.25$	$-0.084 < g_* < 0.096$
$n = +1$	$-0.09 < g_* < 0.05$	$-0.66 < g_* < 0.10$	$-0.07 < g_* < 0.07$	$-0.11 < g_* < 0.12$	$-0.068 < g_* < 0.047$

Correlation function					
Spectral index	CMASS NGC	CMASS SGC	LOWZ NGC	LOWZ SGC	All
$n = -2$	$-0.08 < g_* < 0.07$	$-0.11 < g_* < 0.12$	$-0.11 < g_* < 0.11$	$-0.16 < g_* < 0.22$	$-0.056 < g_* < 0.055$
$n = -1$	$-0.14 < g_* < 0.11$	$-0.14 < g_* < 0.18$	$-0.16 < g_* < 0.15$	$-0.21 < g_* < 0.30$	$-0.086 < g_* < 0.093$
$n = +1$	$-0.10 < g_* < 0.62$	$-0.11 < g_* < 0.14$	$-0.12 < g_* < 0.10$	$-0.14 < g_* < 0.16$	$-0.072 < g_* < 0.066$

Table A2. Same as Table 2 except for the scale-dependence of the quadrupolar modulation, $f(k) = (k/k_0)^n$ with $n = -2, -1, \text{ and } 1$, where the pivot scale is chosen as $k_0 = 0.05 h \text{ Mpc}^{-1}$.

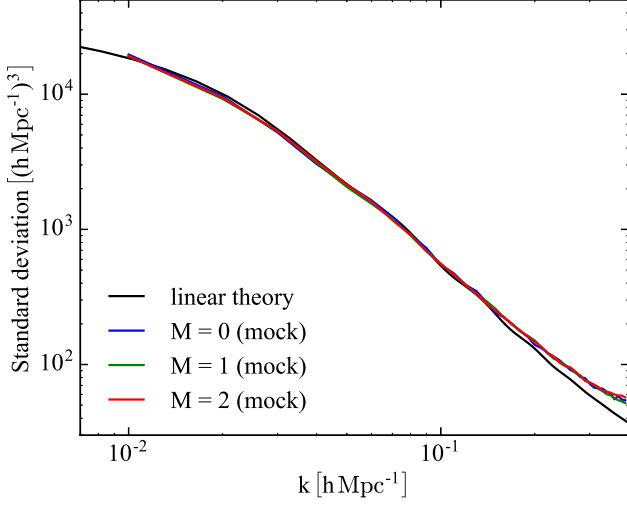


Figure C1. Standard deviations of the BipoSH coefficient P_{20}^{2M} as a function of scales. The colored lines represent the estimates of the standard deviation from the QPM mocks (Section 6.2), and the black line denotes the prediction of the linear theory given by equation (C1).